Lipid acyl chain protrusion induced by the influenza virus hemagglutinin fusion peptide detected by NMR paramagnetic relaxation enhancement

Yijin Zhang, Ujjayini Ghosh, Li Xie, Daniel Holmes, Kathryn G. Severin, David P. Weliky [*]

Department of Chemistry, Michigan State University, East Lansing, MI 48824, USA

ARTICLE INFO

ABSTRACT

The glycoprotein spikes of membrane-enveloped viruses include a subunit that catalyzes fusion (joining) of the viral and target cell membranes. For influenza virus, this is subunit 2 of hemagglutinin which has a ~ 20-residue N-terminal fusion peptide (Fp) region that binds target membrane. An outstanding question is whether there are associated membrane changes important for fusion. Several computational studies have found increased "protrusion" of lipid acyl chains near Fp, i.e. one or more chain carbons are closer to the aqueous region than the headgroup phosphorus. Protrusion may accelerate initial joining of outer leaflets of the two membranes into a stalk intermediate. In this study, higher protrusion probability in membrane with vs. without Fp is convincingly detected by larger Mn^{2+}-associated increases in chain ^{13}C NMR transverse relaxation rates (Γ_2's). Data analysis provides a ratio $\Gamma_{2,neighbor}/\Gamma_{2,distant}$ for lipids neighboring vs. more distant from the Fp. The calculated ratio depends on the number of Fp-neighboring lipids and the experimentally-derived range of 4 to 24 matches the range of increased protrusion probabilities from different simulations. For samples either with or without Fp, the Γ_2 values are well-fitted by an exponential decay as the ^{13}C site moves closer to the chain terminus. The decays correlate with free-energy of protrusion proportional to the number of protruded -CH_2 groups, with free energy per -CH_2 of ~0.25 k_BT. The NMR data support one major fusion role of the Fp to be much greater protrusion of lipid chains, with highest protrusion probability for chain regions closest to the headgroups.

1. Introduction

Many zoonotic diseases including AIDS, influenza, and COVID are caused by viral pathogens that are membrane-enveloped [1–5]. An initial step in cellular infection is fusion (joining) of the viral and target cell membranes with consequent deposition of the viral capsid in the cytoplasm. Enveloped viruses have glycoprotein spikes whose protein have a receptor-binding subunit (RbSu) followed by a fusion subunit (FsSu), with typical proteolytic cleavage between the two subunits [1,6–10]. The FsSu has a single transmembrane domain and a large N-terminal ectodomain (Ed) outside the virus membrane. Each spike contains a core with a defined number (often 3) of non-covalently-associated Ed's of FsSu's, and the same number of RbSu's that are non-covalently bound with this core. After the virus is in the host, RbSu's bind to specific receptor molecules on the exterior of target cells, and for some viruses, there is subsequent endocytosis. The RbSu's move away from the FsSu Ed core, and the core changes to a new structure, typically a thermostable trimer-of-hairpins with $T_m > 90$ °C [11–15]. There isn't sequence homology among the RbSu's of different virus families which can be partly understood because the RbSu's of different virus families bind different molecules. More surprisingly, there also isn't sequence homology or sequence-length homology among the

---

FsSu's of different virus families. As noted above, the final Ed structure is typically a hairpin, but there are substantial length and structural differences between the hairpins of different families [16–20].

There are also large geometric changes of the membranes during fusion, including intermediate structures, but there aren't yet clear experimental data about the relative timings of changes in membrane vs. FsSu Ed structure. Fig. 1 displays a common model for the membrane changes. These changes are in time-sequence: (**a**) initial close (nm) apposition of the viral and target membranes; (**b**) stalk intermediate that connects and is contiguous with the outer leaflets of the two membranes; (**c**) hemifusion diaphragm with contiguous inner leaflets of the two membranes; (**d**) pore formation in the diaphragm; and (**e**) pore expansion with final state of contiguous membranes and viral contents in the cytoplasm [4,21,22]. There are some experimental data that support this model as well as computational studies. The computational consensus estimates for energy barriers of uncatalyzed fusion are ~25 kcal/mol for step **a** and ~ 10 kcal/mol between the step **a** → **b**, **b** → **c**, and **c** → **d** states [4].

FsSu's have a N-terminal region (Ntr) that is not part of the final hairpin structure. The Ntr is often folded within the initial spike and then released as the hairpin forms [6–10]. The Ntr length varies among FsSu's from different viral families, and the range of lengths is typically between 30 and 250 residues. Within a Ntr, there are one or more proposed "fusion peptide" segments that are hypothesized to bind the target membrane during fusion [23–26]. The membrane-bound fusion peptide(s) may reduce the 25 kcal/mol apposition barrier, in conjunction with the more C-terminal hairpin structure of the Ed and viral transmembrane domain. In addition, a membrane may be modified by fusion peptide so that there is also reduction in the 10 kcal/mol barriers between subsequent membrane intermediates [27–38]. A fusion peptide segment has typically been identified by observation of mutations that reduce viral fusion and/or infection without affecting initial spike structure [15,24,39–44]. In addition, a fusion peptide sequence is typically highly-conserved and should bind membrane [41,42,45,46].

The present study is specifically focused on the fusion peptide (Fp) of the influenza virus FsSu which is subunit 2 of the hemagglutinin protein (Ha2). The influenza RbSu (Ha1) binds sialic acid followed by endocytosis of the virus and then endosome maturation that includes pH reduction to ~5 [1]. At low pH, Ha1 separates from the Ha2 Ed and the Ed then changes to the final trimer-of-hairpins structure with accompanying fusion between the viral and endosome membranes. The Ha2 Fp is the ~20 N-terminal and highly-conserved residues of Ha2. The Fp has been identified by: (1) significant attenuation of fusion when specific Fp residues are mutated; (2) very high sequence conservation among different influenza subtypes; and (3) observation of membrane-bound Fp after influenza virus fusion [15,23,40,44,46]. The Ha2 Fp often adopts helical hairpin structure and is a mixture of: (i) closed structure in which the two antiparallel helices are in van der Waals contact; and (ii) semi-closed structure in which the Phe-9 sidechain is inserted between the two helices [47,48].

The effects of the Ha2 Fp on membrane have been studied by computer simulations by several different groups. These simulations have typically been done using a membrane with Fp peptide without the rest of Ha2. One commonly-observed effect is a higher (~4–20×) probability for chain protrusion by lipids next to vs. further from the Fp (Fig. 2) [49–51]. Protrusion is specifically defined as one or more carbons of the lipid chain being at least 1 Å closer to the aqueous phase than the P nucleus of the lipid headgroup. Protrusion is a functionally-interesting motion. As depicted in Fig. 1, an early fusion step is the topological transition from (**a**) initial apposition of viral and target membranes to (**b**) stalk that connects the two membranes and is contiguous with the outer leaflets of these membranes. This step requires protrusion by some outer leaflet lipids of both membranes. The hypothesized correlation between increased lipid chain protrusion near Fp and stalk formation is supported by coarse-grained computer simulations of fusion that begin with full-length Ha2 with final trimer-of-hairpins structure and with Fp's in one membrane and transmembrane domains in the other membrane [52]. In the absence of Fp, simulations show that at any given time, ~1% of the lipids have a protruded chain [49–51]. For simulations with Fp, ~ 4–20× increased protrusion probability is observed for both chains of a lipid that is Fp-adjacent and for a variety of Fp structures [49–51]. Both interfacial and transmembrane locations of the Fp have been observed as well as a variety of geometries of the protruded lipid relative to the Fp. These include: (1) "straddling" of the protruded chain over the Fp; and (2) hydrogen bonding between the headgroup phosphate oxygen and one of the four N-terminal residues of the Fp with associated headgroup intrusion into the bilayer [49,50].

Despite its potential significance, to our knowledge there hasn't yet been direct experimental observation of increased lipid protrusion for membrane with vs. without Fp. If chain protrusion is increased with Fp, there will be associated decreases in chain order parameters, and such decreases were observed and quantified in some of the computational

Membrane fusion model
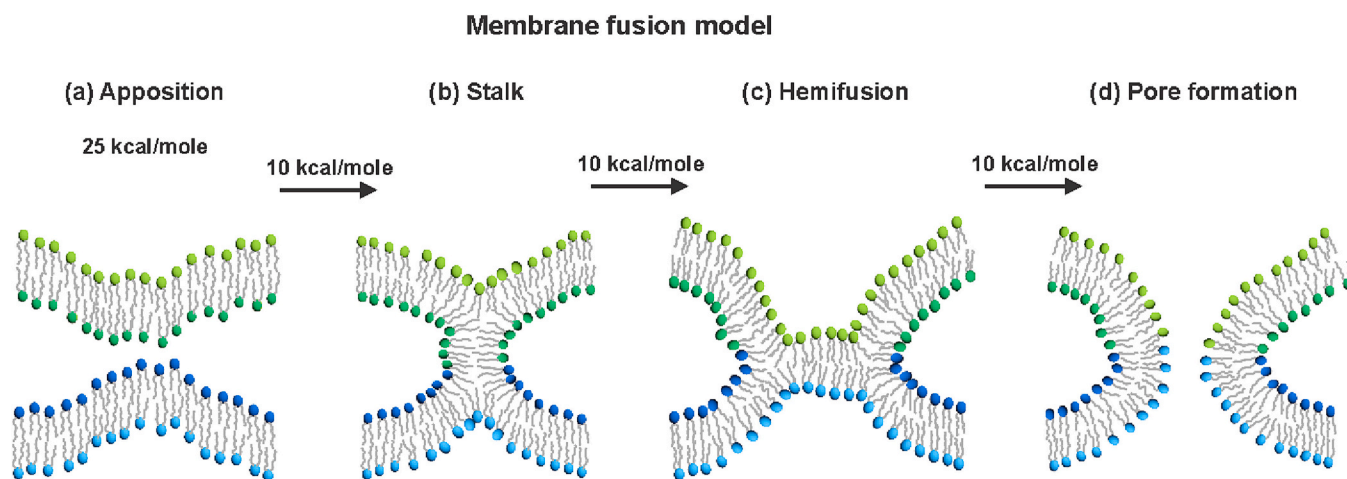
Fig. 1. Pictorial representation of a common membrane fusion model that includes (**a**) initial close apposition of the viral and target membranes; (**b**) stalk formed from the outer leaflets of the two membranes; (**c**) hemifusion diaphragm that is contiguous with the inner leaflets of the two membranes; and (**d**) pore formation. The estimates of the free energy barriers for membrane apposition and for transformation between membrane intermediates are from computational studies of uncatalyzed fusion. The figure doesn't show the final step of pore expansion that precedes full contents mixing. The different colors of the headgroups are meant to visually enhance the changes in membrane topology during fusion but don't describe the locations of specific lipids during fusion. During the ~20 s estimated lifetime of a membrane intermediate structure in viral fusion, a lipid molecule could diffuse over ~10^{10} Å^2 leaflet area.
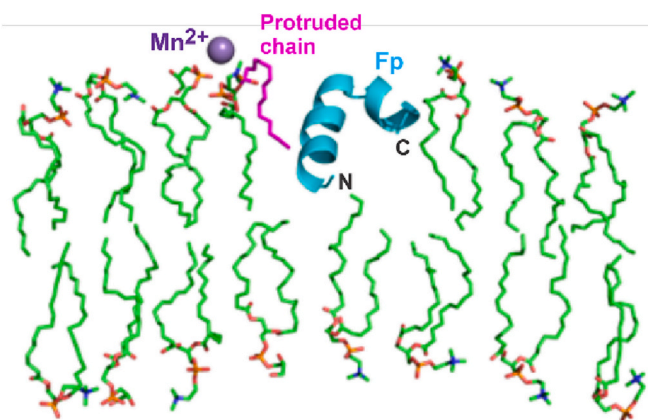
Fig. 2. Representative picture of lipid acyl chain protrusion near a Fp. A set of 128 POPC and 32 POPG lipids in a pre-assembled bilayer were energy-minimized in a water box using the CHARMM/Membrane Builder/Bilayer Builder/Membrane Only System molecular dynamics program. A membrane cross-section is displayed with lipid acyl chains in light green. A representative protruded chain in magenta is next to a Fp backbone in turquoise and near a Mn^{2+} in purple that is bound to a lipid headgroup. The picture shows a protruded palmitoyl chain and a Fp with semi-closed structure with marked N- and C- termini. There is increased protrusion in simulations for both palmitoyl and oleoyl chains and for lipids next to a variety of Fp structures. In addition, Fp in simulations is observed with both interfacial and transmembrane locations and protruded lipids exhibit a variety of geometries relative to the neighboring Fp. (For interpretation of the references to colour in this figure legend, the reader is referred to the web version of this article.)

simulations with membrane with Fp peptide [49,51]. However, these computational predictions were contradicted by electron paramagnetic resonance (EPR) and fluorescence spectra that showed increases in chain order parameters for samples with Fp [28,33]. Such increases were also observed for membrane with putative fusion peptides from other virus families [34–36]. The sequences are non-homologous with the Ha2 Fp sequence. However, more recently, ^2H nuclear magnetic resonance (NMR) spectra of membrane with perdeuterated lipids showed decreases in chain order parameters with vs. without Fp [37]. The NMR-derived order parameters were in semi-quantitative agreement with the simulation-derived parameters [49,51,53]. The seeming contradiction between EPR and NMR/simulation may be explained by: (i) EPR detects order for the spin labels and only 0.005 mol fraction of the sample lipids are spin-labeled, whereas (ii) NMR and simulation detect order for all lipids in the sample. The EPR-detected ordering of the spin label with Fp

may be due to preferential binding of Fp to the spin label. This hypothesis is supported by the dose response of ordering with respect to Fp mole fraction. The ordering reaches its maximum value when the Fp: lipid mole ratio ≈ 0.002, which is similar to the spin-labeled lipid:total lipid mole ratio.

There is other indirect experimental support for increased lipid protrusion from analysis of the large increases in ^2H NMR transverse relaxation rates (R_2's) of deuterated lipids in samples with vs. without Fp [38]. The increases are interpreted to be due to modulation of the ^2H NMR frequency as the lipid laterally diffuses in the membrane leaflet. For lipid next to vs. further from Fp, there are larger vs. smaller amplitudes of mean-squared ^2H quadrupolar fields that are correlated with the smaller vs. larger chain order parameters. The experimental increases in R_2's with vs. without Fp are in semi-quantitative agreement with values calculated using experimentally-based estimates of order parameters and the time for a lipid to diffuse past a Fp. Both the decreases in chain ^2H order parameters and large increases in ^2H R_2's were also observed for a membrane sample with the putative fusion peptide of the HIV FsSu (gp41) [38]. The gp41 fusion peptide and the Ha2 Fp have non-homologous sequences and also adopt very different membrane-bound structures [54–58].

Although these earlier experimental data are consistent with increased chain motion for lipid next to vs. further from Fp, they don't directly evidence increased protrusion (Fig. 2). This knowledge gap motivated the present experimental NMR study in which chain protrusion is probed using comparison of chain ^{13}C R_2's in samples with vs. without the paramagnetic Mn^{2+} species [59–61]. The Mn^{2+} binds to the phosphate oxygens of the lipid headgroup, so a chain ^{13}C R_2 is augmented when the ^{13}C site is protruded into the headgroup region. The change in protrusion probability with vs. without Fp is probed by the difference in Mn^{2+}-associated increase in R_2, i.e. paramagnetic relaxation enhancement (PRE). There is spectral resolution of some of the NMR signals from different -CH_2 sites, so the approach also yields information about how Fp affects protrusion for -CH_2 groups closer to the headgroup vs. the chain terminus [62].

2. Materials and methods

2.1. Lipids and Fp

Fig. 3 displays the lipids 1-palmitoyl-2-oleoyl-glycero-3-phospho-choline (POPC) and1-palmitoyl-2-oleoyl-sn-glycero-3-phospho-(1′-rac-glycerol) (sodium salt) (POPG) that were purchased from Avanti Polar Lipids (Alabaster, AL, USA). The influenza Ha2 Fp was purchased from GL Biochem (Shanghai, China). Other materials were typically
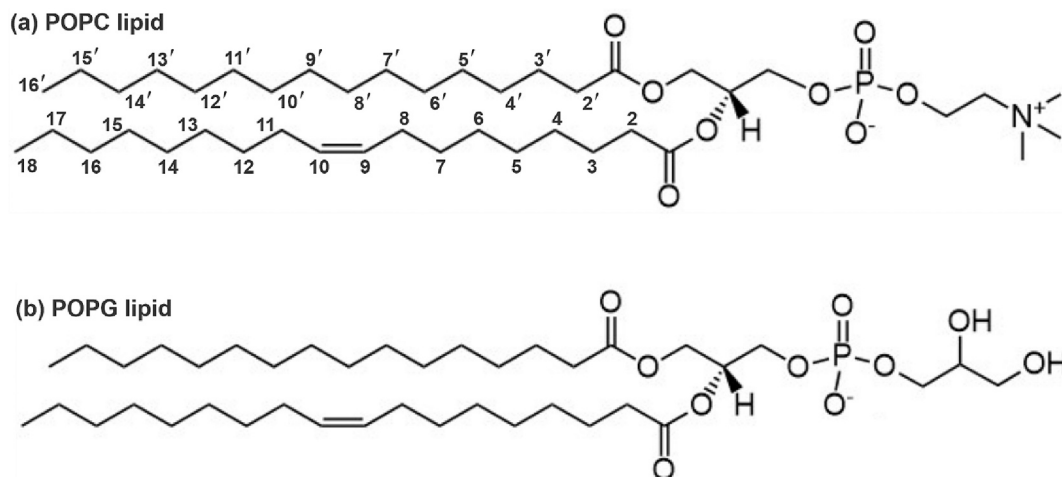

Fig. 3. Chemical structures of POPC and POPG lipids with site numbering of the acyl chains with prime (′) for the palmitoyl chain and no prime for the oleoyl chain.

CP-MAS/Hahn-echo sequence
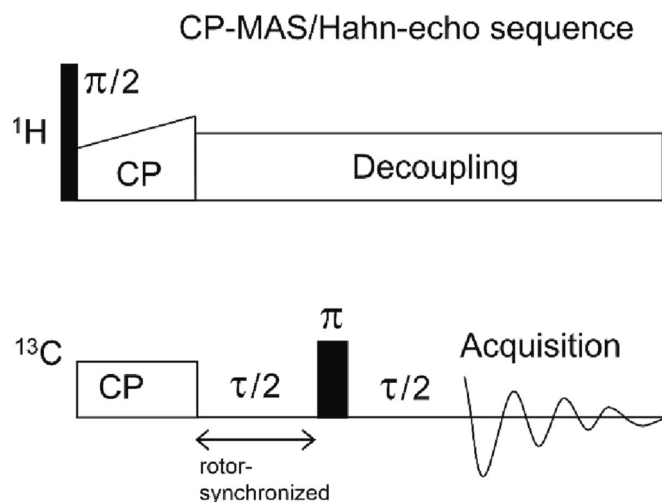
Fig. 4. CP-MAS/Hahn-echo sequence displayed as rf field vs. time. Typical parameters included ^{1}H transmitter at 3.5 ppm, ^{13}C transmitter at 100.0 ppm, 8.0 kHz MAS frequency, 2.5 μs ^{1}H π/2 pulse, 1.4 ms CP contact time, an array of τ between ~2 and ~40 ms with τ/2 an integral number of rotor periods, 10.0 μs ^{13}C π pulse, SPINAL-64 ^{1}H decoupling during the Hahn-echo and acquisition periods, ^{13}C acquisition with 25 μs dwell time and 1400 complex points, 1 s recycle delay, and sum of 8 or 16 K acquisitions using the phase cycle described in the text. Typical ^{1}H rf fields are: CP, linear ramp between 44 and 60 kHz; and decoupling, 50 kHz. The typical ^{13}C CP rf field is 42 kHz.

purchased from Sigma-Aldrich (St. Louis, MO). The Fp sequence is GLFGAIAGFIENGWEGMIDGGGKKKKG. The underlined segment is the 20 N-terminal residues of the Ha2 subunit of the hemagglutinin protein (H3 subtype) and the C-terminal segment is non-native residues that greatly increase Fp solubility in aqueous solution so that Fp binding to membrane can be done without organic solvent or detergent additives. The Fp was prepared by Fmoc solid-phase peptide synthesis and purified by reverse-phase HPLC. GL Biochem stated that Fp purity >95% and this statement is consistent with the electrospray ionization mass spectrum that we acquired (Fig. S1).

2.2. Membrane samples

(**1**) Lipid (~50 μmole) was dissolved in 2 mL chloroform:methanol (9:1 v/v) and the solvent removed by nitrogen gas and then overnight vacuum. (**2**) The dried lipid was suspended in ~2 mL of 10 mM HEPES/5 mM MES buffer at pH 5.0 and the suspension was subjected to freeze-thaw cycles (~10×). (**3**) The suspension was subjected to ultra-centrifugation at 150000 *g* at 4 °C for 2 h. (**4**) The harvested lipid pellet was lyophilized. (**5**) A hydrated lipid sample was prepared in a 3.2 mm outer-diameter NMR rotor by adding in sequence a ~ 10 μL aliquot of water, a portion of the lipid pellet, and then another aliquot of water. The total volume was ~40 μL. The top cap was placed on the rotor followed by overnight incubation at ambient temperature for membrane hydration. Evidence for hydration includes wet appearance and reproducible ^{13}C NMR linewidths (~0.3 ppm full-width at half-maximum).

2.3. Membrane samples with Mn^{2+}

An aqueous solution was prepared with $[MnCl_2]$ either ~40 mM or ~4 mM and an aliquot added to the lipid suspension after step **2**. The suspension was then subjected to freeze-thaw cycles (~5×) to promote homogeneous distribution of Mn^{2+} in the sample [60]. After step **3** ultracentrifugation, $[Mn^{2+}]_{free}$ was detected in the supernatant using an Agilent/Varian AA240 atomic absorption spectrometer with air-acetylene flame and 279.5 nm wavelength. Instrument calibration was done with $MnCl_2$ standard solutions in HEPES/MES buffer at pH 5. The

Mn^{2+} not in the supernatant was considered bound to the membrane and %Mn^{2+} = (mole bound Mn^{2+})/(mole lipid) × 100.

2.4. Membrane samples with Fp

A solution was prepared with [Fp] ≈ 1 mM in HEPES/MES buffer at pH 5.0. The solution was added dropwise to the lipid suspension after step **2** so that the Fp:lipid ≈ 1:30 mole:mole ratio. The Fp/lipid suspension was subjected to freeze/thaw cycles (~5×) and then gently agitated overnight. If Mn^{2+} was to be included in the sample, the $MnCl_2$ solution was added before the freeze/thaw cycles. After step **3** ultra-centrifugation, $[Fp]_{free}$ was measured in the supernatant using A_{280} and if $MnCl_2$ had been added, $[Mn^{2+}]_{free}$ was measured in the supernatant using flame atomic absorption spectroscopy.

2.5. NMR spectroscopy

Data were acquired on a NMR spectrometer with 9.4 T magnet, Bruker Neo console, and Bruker Efree magic angle spinning (MAS) probe designed for lower dielectric heating of aqueous samples and for a rotor with 3.2 mm outer diameter. NMR data were acquired at 298 K with 8.0 kHz MAS frequency, ^{13}C transmitter at 100.0 ppm, and ^{1}H transmitter at 3.5 ppm. Fig. 4 displays the pulse sequence with ^{1}H → ^{13}C cross polarization (CP) followed by dephasing with Hahn echo, and then ^{13}C acquisition, with ^{1}H decoupling during dephasing and acquisition [63,64]. CP parameters were varied to yield highest aliphatic intensity and typically included a 2.5 μs ^{1}H π/2 pulse followed by 1.4 ms contact time with 42 kHz ^{1}C radiofrequency (rf) field and ^{1}H rf field with a linear ramp between 44 and 60 kHz. The Hahn echo was τ/2-^{13}C π pulse-τ/2. Data were collected for a range of τ typically between ~2 and ~40 ms and the 10.0 μs ^{13}C π pulse was rotor-synchronized with the start of dephasing. There was 50 kHz rf field of the ^{1}H SPINAL-64 decoupling, acquisition with 25 μs dwell time and 1400 complex points, 1 s recycle delay, and sum of 8 or 16 K scans. The phases of ^{1}H π/2, ^{13}C CP, ^{13}C π, and receiver were cycled: (y, x, x, x); (−y, x, −x, −x); (y, −x, −x, −x); (−y, −x, x, x); (y, y, y, y); (−y, y, −y, −y); (y, −y, −y, −y); (−y, −y, y, y). The 8-step phase cycle includes 180° alternation of the ^{1}H π/2 phase and correlated quadrature alternation of the ^{13}C CP, ^{13}C π, and receiver phases. Spectra were referenced using the methylene peak of adamantane at 40.5 ppm peak and the terminal lipid chain ^{13}CH$_3$ peak at 13.9 ppm.

The ^{1}H recycle delay of 1 s was chosen based on earlier studies that showed the ^{1}H longitudinal relaxation rate is ~1.6 s^{-1} for lipid -CH$_2$ groups in the liquid-crystalline phase [65,66]. The 1 s recycle delay is close to the ~0.8 s delay for optimal (signal-to-noise)/time. Longer ^{1}H recycle delay results in larger initial ^{1}H magnetization for ^{1}H-^{13}C cross-polarization, but because the same delay is used throughout a data array, all the ^{13}C intensities from the array are scaled by the same factor, and there isn't an effect on the ^{13}C R_2 transverse relaxation rate.

The NMR data were typically processed with 8 K zero-filling, 20 Hz exponential line broadening, Fourier transform, zero- and first-order phase correction, and baseline correction. Spectral peaks were integrated over specific chemical shift ranges and the peak integrals S vs. τ were fitted to S = A × exp.($−R_2 × τ$) with A and R_2 as fitting parameters.

3. Results

3.1. NMR sample preparation

The goal of this study is to probe whether or not lipid acyl chains have greater probability of protrusion into the aqueous phase when Fp is membrane-bound, as has been observed in some simulations. There are several considerations for sample preparation including lipid composition of the membrane and optimal mole% values of membrane-bound Fp and Mn^{2+}, where %Fp or %Mn^{2+} = (mole Fp or Mn^{2+})/(mole lipid) × 100. One consideration for %Fp is simulation data showing that

protrusion probability is increased by a factor of 4–20× for lipids next to a Fp, whereas changes are much smaller for more distant lipids [49–51]. During NMR data collection, a lipid molecule experiences rapid lateral diffusion in the liquid-crystalline phase and will spend time both next to and further from a Fp [67–69]. Larger %Fp is anticipated to result in greater fraction of time next to Fp but there will also be undesired effects if %Fp is too large. These include oligomeric β sheet rather than monomer helical hairpin Fp structure, with the latter being the likely Fp structure in full-length Ha2 [15,70]. For the 3% Fp of our samples, earlier studies evidence that the Fp adopts monomer helical hairpin structure and the membrane retains the liquid-crystalline bilayer phase [29,37,38,48,71,72]. This retention was supported by comparison between lipid samples without vs. with Fp. The two sample types exhibited similar lineshapes, linewidths, and relaxation rates for both their ^{31}P and ^{2}H static NMR spectra.

We first prepared POPC samples because the earlier simulations had typically used POPC. For sample preparation with an aliquot corresponding to 5% Mn^{2+}, the $[Mn^{2+}]_{free} \approx 0$ in the supernatant after centrifugation which correlates with ~5% bound Mn^{2+}, i.e. complete binding to lipid. By contrast, most Mn^{2+} did not bind to POPC with 3% bound Fp. The low binding may be due to electrostatic repulsion between Mn^{2+} and Fp, where the calculated Fp charge is +1.6. We switched to POPC:POPG (4:1), referred to as "PC:PG", with the choice of POPG based on its −1 charge and on otherwise similar properties to POPC [73]. For sample preparation with an aliquot corresponding to 5% Mn^{2+}, the $[Mn^{2+}]_{free}$ correlated with ~5% bound Mn^{2+} for PC:PG without Fp and ~ 4% bound Mn^{2+} for PC:PG with 3% Fp. For PC:PG either without or with Mn^{2+}, there was complete binding of Fp to lipid, based on $A_{280} \approx 0$ in the supernatant after centrifugation. This result is consistent with $Fp_{bound}:Fp_{free} \approx 10^4$ calculated by $K_{bind} \times$ [lipid] where $K_{bind} \approx 10^6$ M^{-1} is the previously-determined binding constant and [lipid] $\approx 10^{-2}$ M in our sample preparation [25].

^{13}C CP NMR spectra without Hahn echo are displayed for the lipid samples in Fig. 5 either (a) without or (c) with Fp. Assignments are shown for the lipid acyl chain peaks use the Fig. 3 carbon numbering with prime (′) for the palmitoyl chain and no prime for the oleoyl chain [62]. There typically isn't resolution of individual peaks for POPC vs. POPG. There are resolved peaks for sites with distinctive bonding environments, but with superposition of signals from at least two sites. The 9,10 peak exhibits partial resolution of the 9 and 10 signals at higher and lower shift, respectively. The * peak is a superposition of signals from the 4–7, 12–15, and 4′-13′ sites. For the same lipid site peak, there are negligible spectral shift or width differences for samples without vs. with Fp. There aren't peaks that could correspond to Fp signals, with possible explanations being the: (1) 3% Fp concentration; and (2) broader Fp linewidths because of less motional averaging for Fp vs. lipid.

We first measured the effect of %Mn^{2+} on ^{13}C R_2, with the goal of finding the optimal %Mn^{2+} for detection of lipid protrusion using the R_2 difference between samples with vs. without Mn^{2+}, i.e. $\Gamma_2 = R_{2,Mn} - R_{2,NoMn}$. The Fp effect on protrusion is assessed by comparison of $\Gamma_{2,Fp}$ vs. $\Gamma_{2,noFp}$. The Mn^{2+} is likely close to the negatively-charged lipid phosphate oxygens in a lipid headgroup. The $\Gamma_2 \propto \langle r^{-6} \rangle$ where r is the ^{13}C-Mn^{2+} distance and $\langle ... \rangle$ is the average over the ~10 ms NMR measurement time [59]. The $\langle r^{-6} \rangle$ will depend on %Mn^{2+} as well as lipid ^{13}C site (Figs. 2, 3). We hypothesized that increased lipid protrusion with Fp could be mostly clearly observed if $\Gamma_{2,noFp}$ were comparable or smaller than $R_{2,noMn,noFp}$. This is based on the idea that Fp-induced increases in $\langle r^{-6} \rangle$ would be more readily detectable if $\Gamma_{2,noFp}$ isn't already approaching its maximal value. We first tried 5% Mn^{2+} in lipid without Fp and observed complete loss of the 2,2′ and 3,3′ signals as well as apparent $\Gamma_2/R_{2,noMn}$ ratios of ~10 for 8,11 and 9,10, ~6 for *, and ~ 5 for 16,14′. We then investigated %Mn^{2+} in the 0.5–1.25% range and observed that even at 0.5%, $\Gamma_2 > 0$ for many peaks and $\Gamma_2/R_2 < 1$ for all peaks (Tables 1, S1, and S2). We then prepared samples with 0.5% Mn^{2+} for more complete analysis. There was no detectable $[Mn^{2+}]_{free}$ for the lipid without Fp sample and small $[Mn^{2+}]_{free}$ for the lipid with Fp sample. The %Mn^{2+}_{bound} were 0.50 and 0.48%, respectively.

3.2. ^{13}C NMR spectra and relaxation

Fig. 5 displays the ^{13}C CP NMR spectra without Hahn echo of the (b) lipid + Mn^{2+} and (d) lipid + Fp + Mn^{2+} samples with comparison to the (a, c) samples without Mn^{2+}. The vertical scales of the four spectra have been adjusted so that the * peaks at 30 ppm have the same height. For the same lipid site peak, there is negligible spectral shift without vs. with Mn^{2+}. For both lipid and lipid + Fp, there is attenuation of the lipid 2,2′
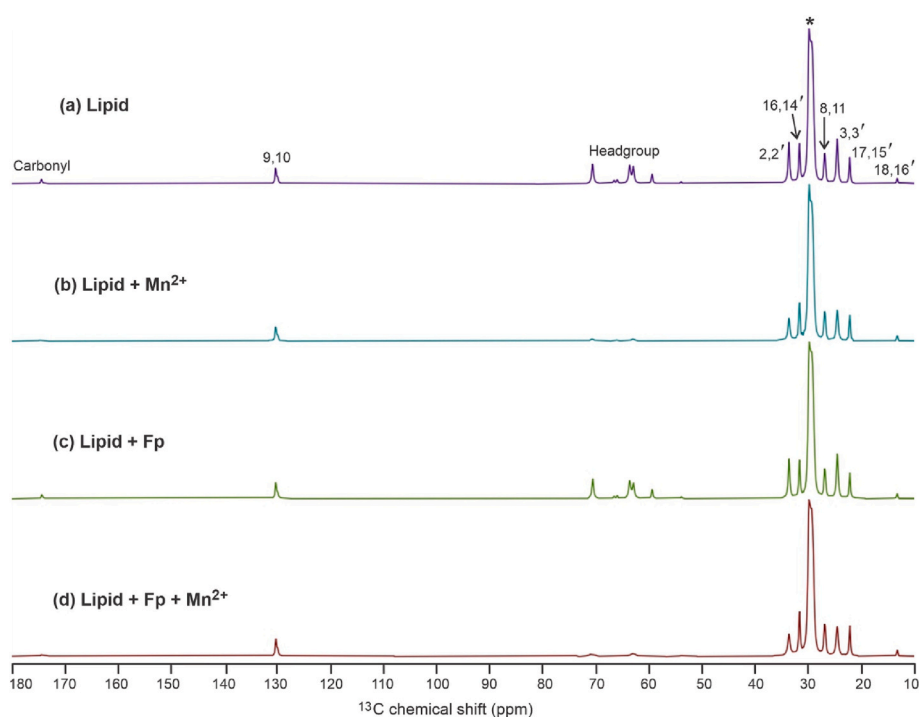
Fig. 5. ^{13}C NMR spectra of samples containing (a) Lipid, (b) Lipid + Mn^{2+}, (c) Lipid + Fp, and (d) Lipid + Fp + Mn^{2+}, with 0.5% Mn^{2+} and 3% Fp that are calculated as (mole Mn^{2+} or Fp)/(mole lipid) × 100. There is POPC:POPG (4:1) lipid composition. The data were acquired after CP without the Hahn echo. The vertical scales of the four spectra have been adjusted so that the "*" peaks at 30 ppm have the same height. Assignments are displayed for the lipid acyl chain peaks use the Fig. 2 carbon numbering with prime (′) for the palmitoyl chain and no prime for the oleoyl chain. There isn't resolution of individual peaks for POPC vs. POPG. There are resolved peaks for sites with distinctive bonding environments, but with superposition of signals from at least two sites. Peaks are assigned for: (1) the 2,2′ and 3,3′ sites that are one and two bonds from the carbonyl groups; (2) the 9,10 C=C and 8,11 C=C adjacent sites of the oleoyl chain; (3) the 18,16′ -CH_3 sites; and (4) the 17,15′ and 16,14′ sites that are one and two bonds from the -CH_3 groups. The * peak is a superposition of signals from the 4–7, 12–15, and 4′-13′ sites. The carbonyl peak and headgroup peak regions are also noted.

Table 1

Site-specific ^{13}C transverse relaxation rates of acyl chains of POPC:POPG (4:1) membrane and % Mn^{2+} dependence (fitting uncertainties in parentheses) [a].

Mn^{2+}	$^{13}C\ R_2\ (s^{-1})$					$^{13}C\ \Gamma_2\ (s^{-1})$			
%	2,2′	3,3′	*	16,14′		2,2′	3,3′	*	16,14′
0	28.1(1.2)	20.3(1.0)	15.9(0.2)	13.9(0.9)					
0.5	50.2(1.8)	34.3(2.2)	20.5(0.9)	15.4(1.0)		22.1(2.5)	14.0(2.4)	4.6(0.9)	1.4(1.3)
0.75	81.9(6.3)	59.1(3.4)	26.4(0.9)	13.7(1.9)		53.8(6.5)	38.8(3.5)	10.5(0.9)	−0.2(2.1)
1.00	92.1(3.4)	60.8(4.6)	28.4(1.5)	22.0(1.4)		64.0(3.8)	40.5(4.7)	12.5(1.5)	8.1(1.6)
1.25	93.9(7.0)	67.8(5.8)	29.2(1.4)	20.7(1.9)		65.8(7.2)	47.6(5.9)	13.3(1.4)	6.8(2.1)

[a] Each ^{13}C transverse relaxation rate (R_2) was determined from best-fitting the integrated NMR peak intensity S vs. delay time τ using $S = A \times \exp.(-R_2 \times \tau)$ where A and R_2 are fitting parameters. The fitting uncertainty of R_2 is given in parentheses. The Γ_2 values are the differences between the best-fit R_2 values of samples with vs. without Mn^{2+}. The * peak is the superposition of the 4–7, 12–15, and 4′-13′ signals. The typical ppm integration ranges for peaks are: 2,2′, 33.00–37.00; 3,3′, 24.00–26.30; *, 28.30–31.50; 16,14′, 31.50–33.00. The % Mn^{2+} = (mole bound Mn^{2+})/(mole lipid) × 100.

and 3,3′ peak intensities with vs. without Mn^{2+}, whereas there is not obvious attenuation for the 16,14′, 17,15′, and 18,16′ peaks. In addition, the lipid headgroup and CO signals are highly attenuated by Mn^{2+}.

Fig. 6 displays 2,2′ spectral signal intensities vs. $\Delta\tau$ (increment in dephasing time) of the four samples. The spectra were acquired with the CP-Hahn echo sequence (Fig. 4). The vertical scales of the spectra of each sample were adjusted so that the $\Delta\tau = 0$ spectral peaks of all samples have the same height. The signal intensities of the (a) lipid and (c) lipid + Fp samples exhibit semi-quantitatively similar attenuation of signal intensities with $\Delta\tau$. There is greater attenuation for the (c) lipid + Mn^{2+} sample and even greater attenuation for the (d) lipid + Fp + Mn^{2+} sample. Fig. 6 provides qualitative spectral evidence which supports the hypothesis that bound Fp induces higher probability of lipid protrusion. Although the shortest τ value was 1.25 ms for panel (a) vs. 2.00 ms for (b-d), the NMR intensity $S(\tau)$ for all data was close to the $S(0)$ intensity prior to relaxation-associated decay, i.e. the $S(\tau)/S(0)$ ratio in (a-d) is ~0.96, 0.90, 0.95, and 0.88, respectively, as calculated using the R_2

rates described in the next paragraph.

The integrated intensities vs. τ of each acyl chain -CH_2 signal were fitted to single exponential decays, i.e. $S(\tau) = A \times \exp.(-R_2 \times \tau)$ where A and R_2 are fitting parameters. Fig. 7 displays plots and fittings of $S(\tau)/A$ vs. τ for some of the signals and Table 2 gives the best-fit R_2's for all fittings as well as the Γ_2's, the R_2 changes for samples with vs. without Mn^{2+}. Table 2 provides the uncertainties in the R_2 and Γ_2 values in parentheses. Fitting is done both for the full integration range of the * peak and for smaller integration ranges of partially-resolved peaks with predominant contributions from a more limited number of sites (Fig. S2). The uncertainties of the experimental peak intensities were calculated as the standard deviations of the integrated intensities in noise regions of the spectra. For two-site peaks, these experimental uncertainties were typically between 10^{-3} and 10^{-2}, i.e. smaller than the dimensions of points in the plots in Fig. 7. Fig. S3 displays the data and fittings on a logarithmic scale. Fig. 8 displays a bar plot of the Γ_2's of samples without vs. with Fp, with data from each of the resolved peaks
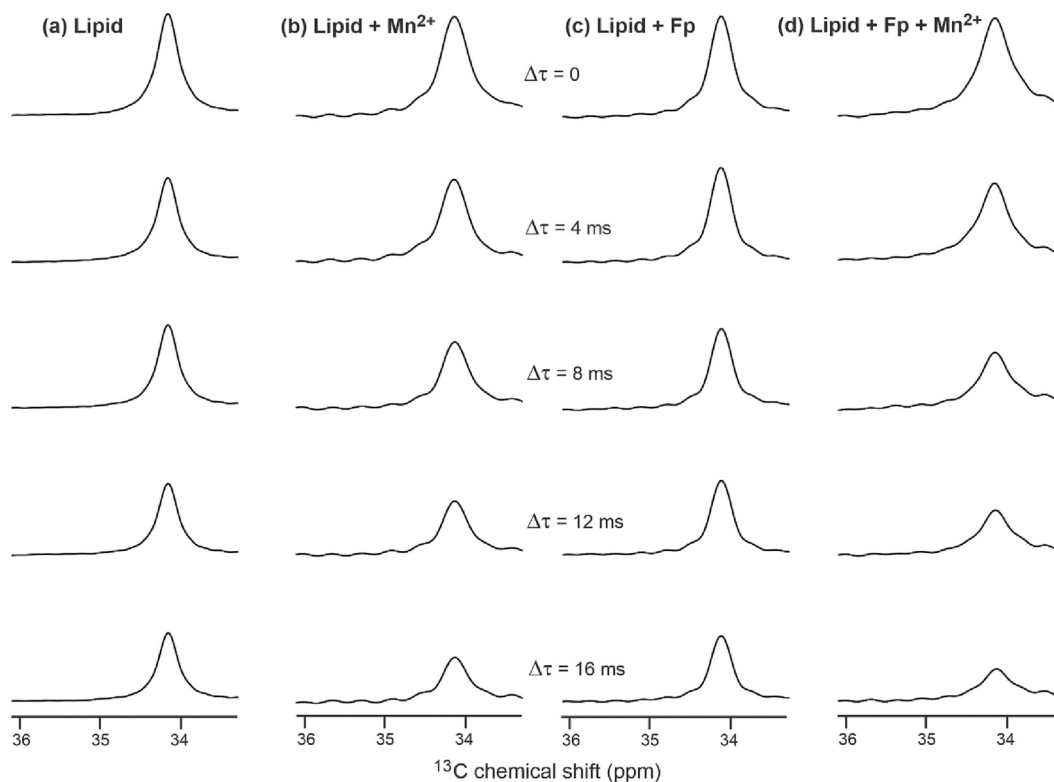
**Fig. 6.** The 2,2′ spectral signals vs. $\Delta\tau$ (increment in dephasing time) of samples containing (a) Lipid, (b) Lipid + Mn^{2+}, (c) Lipid + Fp, and (d) Lipid + Fp + Mn^{2+}, with 0.5% Mn^{2+} and 3% Fp that are based on (mole Mn^{2+} or Fp)/(mole lipid) × 100. Spectra were acquired with the CP-Hahn echo sequence. The vertical scales of the spectra of each sample were adjusted so that the $\Delta\tau = 0$ spectral peaks have the same height. For these top spectra, $\tau = 1.25$ ms for (a) and 2.00 ms for (b-d).
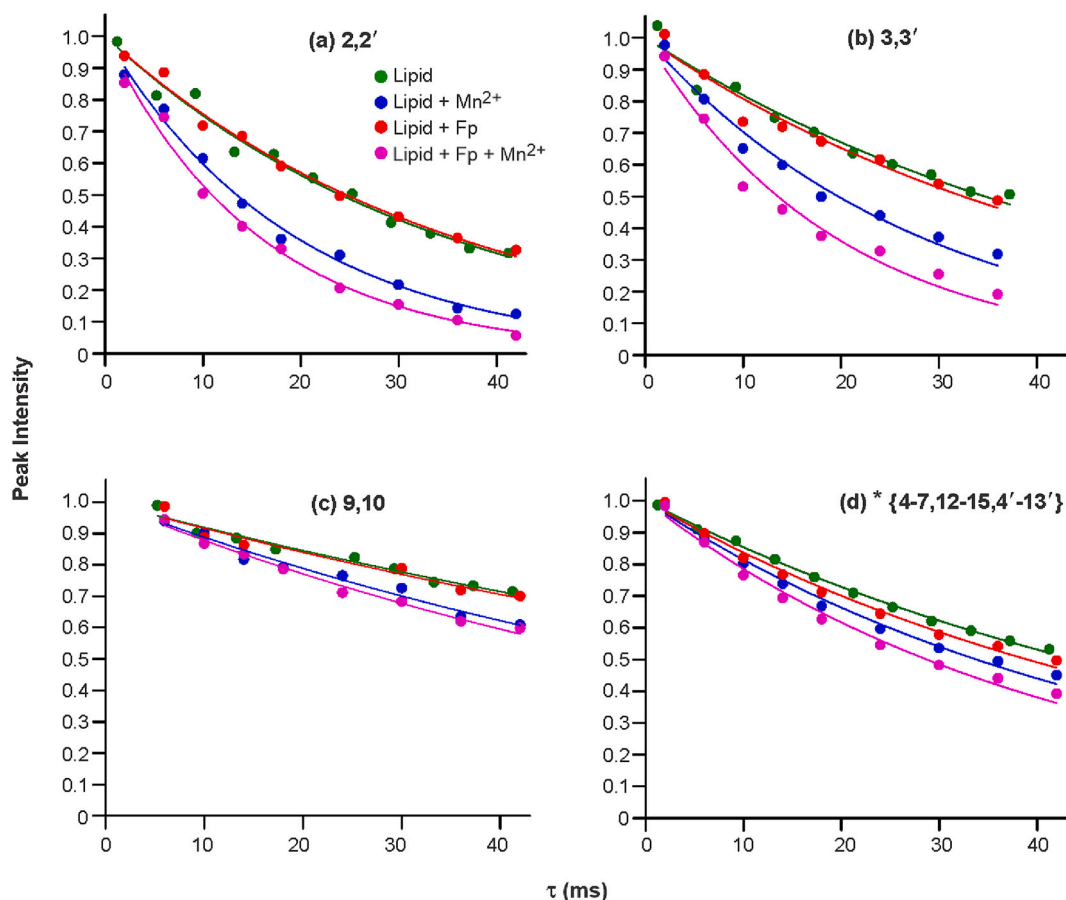
Fig. 7. Integrated peak intensities vs. dephasing time (τ) and best-fit single exponential decays for the Lipid, Lipid + Mn^{2+}, Lipid + Fp, and Lipid + Fp + Mn^{2+} samples. Data and fittings are displayed for the (a) 2,2′; (b) 3,3′; (c) 9,10; and (d) * peaks. The * peak is a superposition of signals from the 4–7, 12–15, and 4′-13′ sites. The peak intensities vs. τ were fitted to $A \times \exp.(-R_2 \times \tau)$ with A and R_2 as fitting parameters. The displayed intensities have been divided by A so that the best-fit intensity = 1 for all peaks when τ = 0. The best-fit R_2's and their uncertainties are presented in Table 2. The uncertainties in the peak intensities were calculated as the RMSD's of ten different integrals in noise regions of the spectra. For the two-site peaks, these uncertainties were typically between 10^{-3} and 10^{-2} and less than the dimension of the points in the plots.

that are due to two ^{13}C sites in the acyl chains (Fig. 5). Table 3 lists the experimental linewidths ($\Delta\nu$'s) of the peaks in the four samples as well as differences $\Delta[\Delta\nu]$ with vs. without Mn^{2+}. Table 4 provides the inhomogeneous contributions to the linewidths of the resolved peaks, calculated using $\Delta\nu_{inhom} = \Delta\nu_{exp} - R_2/\pi$. The $\Delta\nu_{inhom}$ values are shown for resolved peaks of individual samples, along with average values for the four samples and associated standard deviations.

The four samples for Figs. 5-8 were prepared around the same time and as similarly as possible other than the prescribed absence vs. presence of Mn^{2+} and/or Fp. Replicate datasets were acquired and analyzed and Table S3 provides the best-fit R_2's for the replicate data. The differences in best-fit R_2's between replicates are typically comparable to the uncertainties for the differences. Table S4 displays best-fit R_2's for replicate samples and the R_2's are also similar between samples.

4. Discussion

4.1. Hydration and location of Mn^{2+} in samples

The lipids in the samples were likely close to full hydration. Water was added to the rotor both before and after the lipid is added, i.e. the water was initially both underneath and on top of the lipid. The rotor was then sealed with the top cap followed by >12 h prior to acquisition of NMR spectra, and this incubation time was intended to promote water permeation and homogenous hydration of the lipid. Such hydration is

evidenced by the: (1) wet appearance of the sample, including after the NMR experiments were completed; and (2) ^{13}C symmetric lineshapes with narrow (~0.3 ppm FWHM) linewidths. We also anticipate little evaporation of water because the rotor was sealed, the MAS frequency was moderate (8 kHz), and the ^1H rf circuit of the NMR probe was designed to minimize dielectric heating of the water. For a typical sample, ~20 μL water was added to the rotor which has ~40 μL total volume rotor, so there is ~20 μL lipid in the sample. POPC and water have similar densities, so the lipid:water mass ratio was similar to the volume ratio. By this approach, the lipid:water mass ratio in our samples was comparable to the ~3:2 ratio for fully-hydrated lipid, which was calculated using 28 water molecules-per-lipid molecule [74].

The Mn^{2+} likely binds the lipids rather than Fp. As noted in the Results section, membrane with only POPC lipid (with zwitterionic headgroup) quantitatively binds Mn^{2+} whereas POPC membrane with bound Fp doesn't bind Mn^{2+}. This was the reason that the NMR samples were prepared with 20 mol% POPG lipid with anionic headgroup, with resulting Mn^{2+} binding when peptide was also bound. In addition, the experimentally-determined pK_a's of the sidechains of the two Glu and one Asp sidechains are >5 [75]. For the NMR samples at pH 5.0, the Glu and Asp sidechains have only partial negative charge, whereas the lipid headgroups have full negative charge.

Table 2

Site-specific ^{13}C transverse relaxation rates of acyl chains of POPC:POPG (4:1) membrane and Mn^{2+} and Fp dependences (uncertainties in parentheses) [a].

^{13}C	R_2 (s^{-1})					Γ_2 (s^{-1})	
	w/o Fp		3% Fp			w/o Fp	3% Fp
	w/o Mn^{2+}	0.5% Mn^{2+}	w/o Mn^{2+}	0.5% Mn^{2+}			
2,2′	28.8(1.4)	51.5(2.1)	28.1(1.2)	63.5(3.2)		22.8(2.6)	35.4(3.4)
3,3′	20.0(1.5)	35.2(2.4)	21.3(2.0)	51.1(4.0)		15.2(2.8)	29.8(4.1)
8,11	9.1(0.7)	12.6(0.9)	13.6(1.6)	19.8(1.7)		3.5(1.2)	6.2(2.3)
9,10	8.4(0.6)	11.9(0.8)	8.7(1.0)	13.0(1.2)		3.5(1.0)	4.3(1.2)
16,14′	15.5(0.7)	15.0(0.6)	13.8(0.8)	15.4(0.7)		−0.5(0.9)	1.5(1.0)
17,15′	5.9(0.7)	7.3(0.4)	8.6(0.8)	9.7(1.0)		1.4(0.8)	1.1(1.2)
* {4–7,12-15,4′-13′}	15.8(0.3)	20.5(0.9)	17.8(0.7)	24.1(1.1)		4.7(0.9	6.4(1.3
*1 {6′-9′}	24.8(0.2)	27.2(1.5)	25.4(0.5)	30.3(0.3)		2.5(1.6)	4.9(0.6)
*2 {7,10′,11′}	15.1(0.2)	16.4(0.9)	16.0(0.7)	23.2(1.0)		1.3(0.9)	7.2(1.2)
*3 {4–6,12-15,4′,5′,12′,13′}	11.7(0.3)	18.8(0.9)	15.8(1.2)	23.1(1.8)		7.1(1.0)	7.4(2.2)

[a] Each ^{13}C transverse relaxation rate (R_2) was determined from best-fitting the integrated NMR peak intensity S vs. delay time τ using $S(\tau)$ = A × exp.($-R_2 \times \tau$) where A and R_2 are fitting parameters. The fitting uncertainty of R_2 is given in parentheses. The Γ_2 values are the differences between the best-fit R_2 values of samples with vs. without Mn^{2+}. Typical ppm integration ranges for peaks are: 2,2′, 33.00–37.00; 3,3′, 24.00–26.30; 8,11, 26.50–28.20; 9,10, 128.00–131.00; 16,14′, 31.50–33.00; 17,15′, 21.50–23.60; *, 28.30–31.50; *1, 30.24–31.50; *2, 30.04–30.24; *3, 28.30–30.04 (Fig. S2). The ^{13}C sites that make the largest contributions to the *1, *2, and *3 integration ranges are listed between the brackets. The % Mn^{2+} = (mole bound Mn^{2+})/(mole lipid) × 100. The % Fp is calculated using the same type of expression.
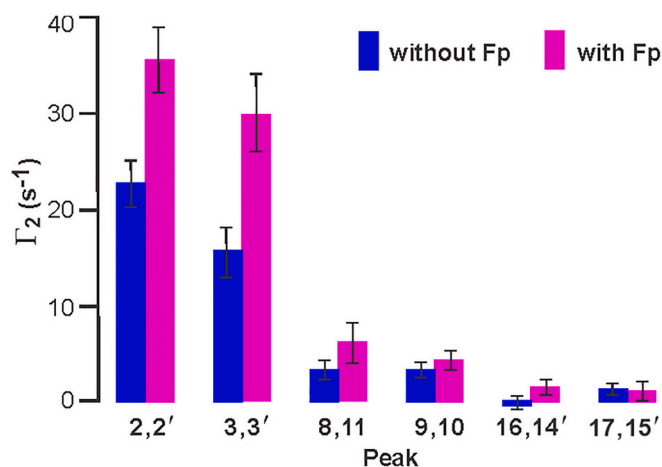

Fig. 8. Bar plot of the Γ_2's, i.e. the differences between the R_2's for samples with vs. without Mn^{2+}. The Γ_2's are displayed for several peaks. Each peak is due to signals from two ^{13}C sites in the acyl chains. The Γ_2's are shown for samples without vs. with Fp. The Γ_2's and their uncertainties are presented numerically in Table 2.

4.2. NMR relaxation data support increased probability of lipid chain protrusion with Fp

There are overall larger Γ_2's for lipid with vs. without Fp, and the magnitude is most pronounced for the 2,2′ and 3,3′ signals, with reductions in R_2 and Γ_2 values for -CH$_2$ sites closer to the chain terminus (Figs. 6-8, Table 2). The Γ_2 trend is consistent with the results of the initial molecular dynamics simulation showing increased protrusion probability with Fp and specifically with the result summarized on p. 3 of this article "…our simulations predict the [Fp] effect on tail protrusion to be most profound in the upper region of the acyl chain …" [49] (Fig. 2).

Earlier NMR relaxation data were used to estimate a correlation time of ~10^{-8} s for the lipid chain motion that could lead to protrusion in the liquid-crystalline membrane [76,77]. This time is much smaller than the

Table 3

Site-specific ^{13}C FWHM NMR linewidths of acyl chains of POPC:POPG (4:1) membrane and Mn^{2+} and Fp dependences [a].

^{13}C	$\Delta\nu$ (Hz)					$\Delta[\Delta\nu]$ (Hz)	
	w/o Fp		3% Fp			w/o Fp	3% Fp
	w/o Mn^{2+}	0.5% Mn^{2+}	w/o Mn^{2+}	0.5% Mn^{2+}			
2,2′	33.1	43.2	34.8	49.4		10.1	14.6
3,3′	37.3	43.1	38.7	47.8		5.8	9.1
8,11	39.7	42.8	38.8	44.1		3.1	5.3
9,10	33.0	39.4	33.7	36.4		6.4	2.7
16,14′	30.0	34.7	30.0	31.1		4.7	1.1
17,15′	27.5	32.9	28.1	28.9		5.4	0.8
* {4–7,12-15,4′-13′}	110.7	112.4	111.7	116.0		1.7	4.3

[a] These are experimental full-width at half-maximum linewidth of the ^{13}C signal of the CP NMR spectrum. The $\Delta[\Delta\nu]$ is the difference in linewidths between samples with vs. without Mn^{2+}.

characteristic ($1/R_2$) ≈ 10^{-1} s for ^{13}C transverse relaxation so the R_2 is most reasonably considered as a weighted average of the chain's high-probability unprotruded state and low-probability protruded state. We hypothesize that a site's Γ_2 is proportional to the probability of chain protrusion (Ω_{prot}) into the headgroup region [61]. This hypothesis is based on: (1) the r^{-6} dependence of Γ_2 where r is the ^{13}C-Mn^{2+} distance; and on (2) smaller r and therefore much larger Γ_2 when the chain is protruded. As described in the Results section, only 0.005 fraction of the lipid headgroups in our samples have bound Mn^{2+}. The Mn^{2+} are likely also exchanging rapidly between headgroups during ^{13}C transverse relaxation. Based on arguments similar to those above for protrusion, we additionally hypothesize that a site's Γ_2 is also proportional to the probability that a Mn^{2+} is bound to a headgroup close to the protruded chain (Ω_{Mn}).

We estimate r for the protruded state with nearby Mn^{2+} by combining our two hypotheses with the known expression for Γ_2 with a nuclear spin I with spin ½ and a nearby paramagnetic species with spin quantum number L:

$$r \approx \left[(1/15) \times (\mu_0/4\pi)^2 \times \gamma_I^2 \times g_e^2 \times \mu_B^2 \times L(L+1) \times (4 J_0 + 3 J_{\omega I}) \times \Omega_{prot} \times \Omega_{Mn} / \Gamma_2 \right]^{1/6} \qquad \text{(Eq. 1)}$$

where μ_0 is the permeability of free space, γ_I is the nuclear spin gyromagnetic ratio, g_e is the electron spin g factor, μ_B is the Bohr magneton, J_ω is the spectral density at angular frequency ω, and ω_I is the angular NMR Larmor frequency of the nucleus [59]. Using the known values of μ_0, γ_I for ^{13}C, g_e, and μ_B, and $L = 5/2$ for Mn^{2+},

$$r \approx \left[(9.106 \times 10^{-45} \, m^6 - s^{-2}) \times (4 J_0 + 3 J_{\omega I}) \times \Omega_{prot} \times \Omega_{Mn} / \Gamma_2 \right]^{1/6} \qquad \text{(Eq. 2)}$$

There are estimates below for the other terms but we note that because of the 6th root dependence, r is fairly insensitive to moderate changes in these estimates, e.g. a $10\times$ increase in the expression in braces correlates with a $1.1\times$ increase in r. The J_ω is calculated using:

$$J_\omega = \tau_c / \left[1 + (\tau_c^2 \times \omega^2) \right] \qquad \text{(Eq. 3)}$$

where τ_c is the correlation time [61]. The $J_0 = \tau_c$ which is much larger than $J_{\omega I}$, based on $\tau_c \approx 10^{-8}$ s, the experimentally-based estimate of the correlation time for chain motion associated with protrusion and on $\omega_I \approx 6 \times 10^8 \, s^{-1}$ [76,77]. We estimate $\Omega_{Mn} \approx 10^{-2}$ based on a protruded ^{13}C being near ~ 2 lipid headgroups and the experimental Mn^{2+} headgroup occupancy ≈ 0.005. For lipid without Fp, $\Omega_{prot} \approx 0.01$ in simulations and the $\Gamma_2 \approx 10 \, s^{-1}$ from our experimental data (Table 2). The resulting calculated $r \approx 4$ Å is plausible for the ^{13}C nuclei of a chain that protrudes into the headgroup region of the membrane.

One notable trend of Fig. 8 and Table 2 is the attenuation of Γ_2 as the ^{13}C site moves closer to the chain terminus. This trend holds for samples both without and with Fp. We have hypothesized that $\Gamma_2 \propto \Omega_{prot}$ and further hypothesize that protrusion of a specific -CH$_2$ group also means protrusion of the -CH$_2$ groups that are closer to the lipid glycerol group. This second hypothesis is based on the location of the glycerol group close to the phosphate group and the chemical bonding of the acyl chain (Fig. 3). For the six ^{13}C NMR signals assigned to two -CH$_2$ sites with sites numbered x and y, respectively (Fig. 5), the average number of protruded -CH$_2$ groups (n) is calculated:

$$n = [(x + y)/2] - 1 \qquad \text{(Eq. 4)}$$

and protrusion of each -CH$_2$ group is hypothesized to require free energy ΔG_{prot} so that Γ_2 depends on n as:

$$\Gamma_2(n) = \Gamma_2(0) \times exp. \left[- \left(n \times \Delta G_{prot} \right) / k_B T \right] \qquad \text{(Eq. 5)}$$

where $\Gamma_2(0)$ is the parameter for the rate when no -CH$_2$ are protruded. Fig. 9 displays fitting with Eq. 5 of the experimental $\Gamma_2(n)$ data vs. n,

with separate fittings of data without and with Fp. The best-fit $\Delta G_{prot}/k_B T$ are 0.249 ± 0.018 without Fp and 0.266 ± 0.016 with Fp. The Eq. 5 model is supported both by the quantitative similarity of the two values and the semi-quantitative agreement with the 0.25–0.50 $k_B T$ range for $\Delta G_{prot}/k_B T$ in one of the simulations [49]. The best-fit $\Gamma_2(0)$ are $27.9 \pm 1.8 \, s^{-1}$ without Fp and $47.3 \pm 2.6 \, s^{-1}$ with Fp.

The molecular dynamics simulations from different groups show that the large enhancement of Ω_{prot} is primarily for lipids next to the Fp whereas the Ω_{prot} of more distant lipids is similar to lipids without Fp. For samples with Fp, the $\sim 10^{-8}$ s time for lateral diffusion of a lipid molecule between Fp-neighboring and more distant locations is much smaller than the $1/R_2$ relaxation time, so the $\Gamma_{2,Fp}$ will be a weighted average of the larger Fp-adjacent and smaller more distant values, $\Gamma_{2,neighbor}$ and $\Gamma_{2,distant}$, respectively. For "q" lipid molecules neighboring a Fp and the ~ 3 mol% Fp of a sample:

$$\Gamma_{2,Fp} = \left(0.03 \times q \times \Gamma_{2,neighbor} \right) + \left[1 - (0.03 \times q) \right] \times \Gamma_{2,distant} \qquad \text{(Eq. 6)}$$

which is algebraically rewritten as:

$$\Gamma_{2,neighbor}/\Gamma_{2,distant} = \left[\Gamma_{2,Fp}/\Gamma_{2,distant} - 1 + (0.03 \times q) \right]/(0.03 \times q) \qquad \text{(Eq. 7)}$$

Using the best-fit $\Gamma_{2,Fp}(0)$ and $\Gamma_{2,noFp}(0)$ values and the approximation $\Gamma_{2,distant}(0) \approx \Gamma_{2,noFp}(0)$:

$$\Gamma_{2,neighbor}/\Gamma_{2,distant} = \left[\Gamma_{2,Fp}(0)/\Gamma_{2,noFp}(0) - 1 + (0.03 \times q) \right]/(0.03 \times q) \qquad \text{(Eq. 8)}$$

The $\Gamma_{2,Fp}(0)/\Gamma_{2,noFp}(0) = 1.70 \pm 0.14$. The value of q will depend on the Fp surface area that contacts lipids and this area will vary with location and orientation of the Fp in the membrane. There is also the possibility that q is reduced because increased protrusion probability is mostly for a subset of neighboring lipids with spatially-specific Fp interactions. A reasonable possible range of q values is 1 to 8, with q = 8 based on interfacial Fp location and $\sim 4\times$ greater cross-sectional area for Fp vs. lipid [47,48]. From Eq. 8, $\Gamma_{2,neighbor}/\Gamma_{2,distant} = 24.3 \pm 4.8$ for q = 1 and 3.92 ± 0.60 for q = 8. This matches the range of $\Gamma_{2,neighbor}/\Gamma_{2,distant}$ ratios that were observed in different simulations [49–51]. The inverse correlation between the experimentally-derived $\Gamma_{2,neighbor}/\Gamma_{2,distant}$ ratio and q is consistent with the larger simulation-derived $\Gamma_{2,neighbor}/\Gamma_{2,distant}$ ratios for transmembrane vs. membrane surface location of the Fp, and the likely larger Fp lipid-contacting area and q value for the surface location [49,51]. In addition, large $\Gamma_{2,neighbor}/\Gamma_{2,distant}$ is observed in a different simulation in which the effective q ≈ 1 because of the strong correlation between protrusion and a hydrogen bond between one of the four N-terminal residues of the Fp and a lipid phosphate

Table 4

Inhomogeneous contributions to site-specific ^{13}C FWHM NMR linewidths of acyl chains of POPC:POPG (4:1) membrane [a].

^{13}C	$\Delta\nu_{inhom}$ (Hz)				Average
	w/o Fp		3% Fp		
	w/o Mn^{2+}	0.5% Mn^{2+}	w/o Mn^{2+}	0.5% Mn^{2+}	
2,2′	23.9	26.8	25.9	29.2	26.4(1.9)
3,3′	30.9	31.9	31.9	31.5	31.6(0.4)
8,11	36.8	38.8	34.5	37.8	37.0(1.6)
9,10	30.3	35.6	30.9	32.6	31.6(2.0)
16,14′	25.1	29.9	25.6	26.2	27.0(1.9)
17,15′	25.6	30.6	25.4	25.8	26.8(2.2)

[a] The $\Delta\nu_{inhom} = \Delta\nu_{exp} - (R_2/\pi)$ i.e. the difference between the experimental full-width at half-maximum linewidth and the experimental relaxation contribution to the linewidth. The average is for the four samples with the standard deviation in parentheses.
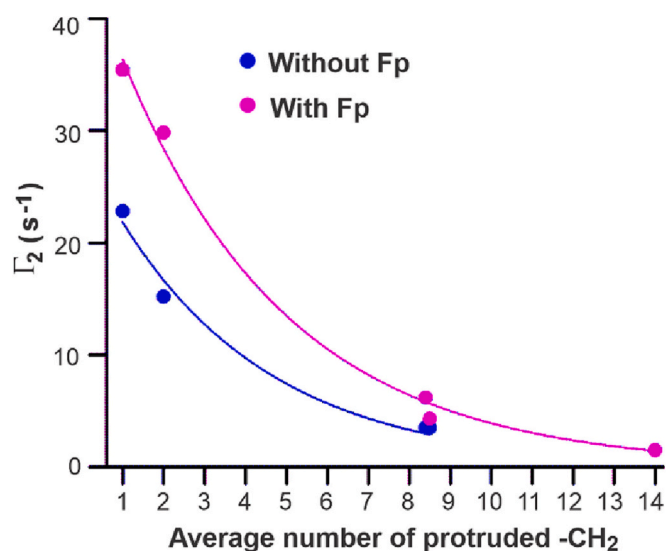
Fig. 9. Plots and exponential decay fittings of Γ_2 vs. average number (n) of protruded -CH$_2$. For each peak corresponding to signals from two -CH$_2$ sites that are numbered x and y (Figs. 3 and 5), this average number is calculated as $[(x + y)/2] - 1$, e.g. 2 for the 3,3′ peak and 14 for the 16,14′ peak. Data are displayed for samples without and with Fp. Separate fittings are done for each sample type using Γ_2 (n) = Γ_2 (0) × exp.(−n × κ) with Γ_2 (0) and κ as fitting parameters and κ = $\Delta G_{prot}/k_B T$. Best-fit values with uncertainties in parentheses are: (1) without Fp, Γ_2 (0) = 27.9(1.8) s^{-1} and κ = 0.249(18); and (2) with Fp, Γ_2 (0) = 47.3(2.6) s^{-1} and κ = 0.266(16).

oxygen, with consequent headgroup intrusion into the membrane interior [50].

Besides the aforementioned simulation observations that increased chain protrusion may be associated with Fp/phosphate hydrogen bonding and headgroup intrusion, protrusion may also be augmented by solvation of lipid chains by hydrophobic Fp sidechains at the membrane surface. This could be part of the basis for much greater Ha2-induced intervesicle lipid mixing at endosomal pH 5.0 vs. physiologic pH 7.4 [15]. This effect is observed with POPC vesicles for which there isn't bulk Ha2/vesicle electrostatic energy. At both pH's, Fp is a mixture of closed and semi-closed helical hairpin structures, and semi-closed has significantly greater hydrophobic surface area [48]. There is higher semi-closed population at pH 5 vs. 7 and therefore larger Fp hydrophobic surface area.

4.3. Linewidth and * peak analysis also support protrusion

For the 2,2′ and 3,3′ signals, there are larger Mn^{2+}-associated increases in linewidth, Δ[Δν], for samples with vs. without Fp (Table 3). The difference is less apparent for two-site signals from ^{13}C nuclei closer to the chain termini, and these observations correlate with the trend of $\Gamma_{2,Fp} - \Gamma_{2,NoFp}$ (Fig. 8 and Table 2). For the two-site signals, Table 4 provides the inhomogenous contributions to linewidths, which are calculated by $\Delta\nu_{inhom} = \Delta\nu - (R_2/\pi)$. Table 4 also provides for each signal the RMSD and average value calculated from the data of the four samples. The typical RMSD is ±2 Hz and the average values are in the 26–37 Hz range. For our spectra, the individual contributions to the signal from each site are typically unresolved, except for 9,10 which has partially-resolved C9 and C10 contributions with respective higher and lower shifts. For earlier ^{13}C NMR spectra of POPC with somewhat narrower linewidths than our spectra, there aren't resolved shift differences (Δδ) between sites for the 2,2′, 16,14′, and 17,15′ signals, and the Δδ are ~0.09, 0.13, and 0.36 ppm for the 3,3′, 8,11, and 9,10 signals, respectively [62]. For the present study, the 2,2′, 16,14′, and 17,15′ signals have $\Delta\nu_{inhom} \approx 27$ Hz which is likely due to 20 Hz exponential line broadening and shimming. There are larger $\Delta\nu_{inhom}$ of ~32 and 37 Hz

for the 3,3′ and 8,11 signals, respectively, and the ~5 and 10 Hz increases over the $\Delta\nu_{inhom} \approx 27$ Hz baseline value correlate semi-quantitatively with the Δδ values of ~9 and ~13 Hz, respectively. For the 9,10 signal, the $\Delta\nu_{inhom} \approx 32$ Hz is smaller than would be expected from the $\Delta\delta \approx 36$ Hz. This anomaly is likely a consequence of the larger C9 vs. C10 contribution to the 9,10 signal. There is greater ^{1}H-^{13}C cross-polarization for C9 vs. C10 because of the smaller vs. larger site mobility that was previously described by differences in site order parameters [62].

The * peak is a superposition of signals from eighteen ^{13}C sites in the middle of the two chains, 4–7, 12–15, and 4′-13′. Table 2 lists the best-fit R_2 and Γ_2 values both for full integration of * intensities and for integration ranges denoted *1, *2, and *3 for which a subset of the ^{13}C sites make the largest contributions, respectively 6′-9′; 7,10′,11′; and 4–6,12-15,4′,5′,12′,13′ [62]. The Γ_2 values from the * fittings are similar to those of 8,11 and 9,10, and are intermediate between the larger 2,2′ and 3,3′ Γ_2 values and smaller 16,14′ and 17,15′ values. The *1 and *2 integrations are dominated by signals from ^{13}C sites closer to CO whereas the *3 integration has large contributions from ^{13}C sites closer to the chain terminus. These different locations correlate with the $\Gamma_{2,Fp} > \Gamma_{2,NoFp}$ for *1 and *2 and for 2,2′; 3,3′; 8,11; and 9,10 fittings, whereas $\Gamma_{2,Fp} \approx \Gamma_{2,NoFp}$ for *3; 16,14′; and 17,15′ fittings. The Mn^{2+}-associated increases of the linewidths of the * peaks are similar to those of resolved ^{13}C sites in the middle and terminal regions of the chains, and the increase for * is a little larger with vs. without Fp (Table 3). The * linewidth has substantial inhomogeneous contribution from the superposition of unresolved signals from many ^{13}C sites.

4.4. Comparison between PRE and other experimental approaches to probe chain motions relevant to fusion

The hypothesis of increased protrusion induced by Fp was initially proposed based on molecular dynamics simulations [49–51]. The typical $\Omega_{prot,NoFp} \approx 0.01$ and the $\Omega_{prot,Fp}$ was larger but still <0.2, i.e. protrusion was always a low-probability state. It is therefore anticipated that the observables from some experimental approaches have large contributions from the high-probability unprotruded chains. The Mn^{2+} paramagnetic relaxation enhancement (PRE) approach of the present study has the advantage that the Γ_2 observable is dominated by the small population of protruded chains, based on: (1) Mn^{2+} is predominantly bound to the lipid headgroup phosphate; (2) the $\langle r^{-6} \rangle$ dependence of Γ_2; and (3) the larger τ_c for protrusion vs. other chain motions [77]. Some other approaches wouldn't have this advantage. As one example, protrusion would also affect lipid ^{13}C-^{31}P dipolar coupling that can be measured by NMR [26]. The coupling is proportional to $\langle \rho^{-3} \rangle$ where ρ is the internuclear distance. For the 2,2′ and 3,3′ sites, the $\langle \rho^{-3} \rangle$ for membrane without vs. with Fp are estimated to be ~2.01 × 10^{-3} vs. ~2.26 × 10^{-3} Å^{-3}, i.e. only ~12% increase, as calculated from $\rho_{C-P,unprot} \approx 8$ Å, $\rho_{C-P,unprot} \approx 5$ Å, $\Omega_{prot,NoFp} \approx 0.01$, and $\Omega_{prot,Fp} \approx 0.05$. Another consideration is that investigation of protrusion by simulation has been done in fluid rather than gel membrane phases, in part because fluid phases are similar to those of membranes in viral fusion. Lipids in fluid phases experience rapid lateral diffusion and also other large-amplitude motions [68,77]. These motions are usually advantageous for the PRE approach because they result in smaller R_2's that can generally be measured more accurately than larger R_2's. The motions also reduce dipolar couplings; however, the NMR spectra often have lower signal-to-noise when measuring smaller vs. larger couplings, so smaller couplings are less accurately-determined [78].

Splay is the term used to describe the large-amplitude movement by the terminal region of the lipid chain into the headgroup region. Splay may be relevant to fusion and has been detected using the ^{1}H-^{1}H NOESY NMR cross-relaxation rate between the terminal methyl and the headgroup nuclei [65]. The NOESY rates have been positively-correlated with the extents of fusion between vesicles with transmembrane peptides [79]. However, these vesicle fusion rates are ~3 × 10^{-4} s^{-1} which

are ~1000× smaller than rates of vesicle fusion induced by Fp's [48]. These results suggest that splay is a less important motion for fusion than the protrusion of chain -CH_2 groups closest to the glycerol linkage, i.e. the motion probed in the present study. This conclusion is supported by the statement on p. 5 of Ref. 49, "…our simulations predict the effect on tail protrusion to be most profound in the upper region of the acyl chain, so a difference in tail exposure might be suboptimal probe for fusion peptide activity." [49]

5. Conclusions

The present study presents convincing experimental data that support a large increase in lipid acyl chain protrusion caused by the membrane-bound Fp domain of the influenza virus Ha2 protein. Increased protrusion had previously been observed in computational simulations and may play an important role in fusion between the viral and the endosome membranes. In particular, protrusion may accelerate the transition from the initial separate apposed membranes to the stalk intermediate that connects and is contiguous with the outer leaflets of the two bodies, Fig. 1a,b. For the present study, protrusion was detected by larger Mn^{2+}-associated increases in transverse relaxation rates of lipid chain ^{13}C nuclei for samples with vs. without Fp. Analysis of the $\Gamma_{2, Fp}$ vs. $\Gamma_{2, NoFp}$ rate increases resulted in a calculated ratio $\Gamma_{2,neighbor}/\Gamma_{2, distant}$ in the range of 4–24 where the ratio is for lipids neighboring vs. more distant from Fp. The ratio values within this range are inversely-correlated with the number of neighboring lipids. The experimental range is similar to the range in simulations for increased protrusion probability of a lipid neighboring vs. more distant from the Fp. For samples either with or without Fp, the Γ_2 values are well-fitted by an exponential decay as the ^{13}C site moves closer to the chain terminus. The decay correlates with a positive free-energy of protrusion that is proportional to the number of protruded -CH_2 groups. The experimentally-determined free energy per -CH_2 is ~0.25 k_BT which matches the value in one of the simulations. Overall, the NMR data support one major fusion role of the Fp to be much greater chain protrusion with highest probability for chain regions closest to the headgroups.

CRediT authorship contribution statement

Yijin Zhang: Conceptualization, Methodology, Software, Validation, Formal analysis, Investigation, Data curation, Writing – original draft, Writing – review & editing, Visualization, Funding acquisition. **Ujjayini Ghosh:** Methodology, Investigation, Writing – review & editing. **Li Xie:** Methodology, Software, Investigation, Writing – review & editing. **Daniel Holmes:** Methodology, Software, Investigation, Writing – review & editing. **Kathryn G. Severin:** Methodology, Software, Resources. **David P. Weliky:** Conceptualization, Methodology, Formal analysis, Writing – original draft, Writing – review & editing, Visualization, Supervision, Project administration, Funding acquisition.

Declaration of Competing Interest

The authors declare that they have no known competing financial interests or personal relationships that could have appeared to influence the work reported in this paper.

Acknowledgements

Appendix A. Supplementary data

Electrospray ionization mass spectrum of Fp; *1, *2, and *3 peak integration ranges; Logarithmic plots and linear fittings; Tables of site-specific ^{13}C R_2's and Γ_2's of acyl chains of POPC:POPG (4:1) membrane and their Mn^{2+} dependences; Tables of relaxation rates from replicate data. Supplementary data to this article can be found online at https://doi.org/10.1016/j.bpc.2023.107028.

References

[1] J.M. White, S.E. Delos, M. Brecher, K. Schornberg, Structures and mechanisms of viral membrane fusion proteins: Multiple variations on a common theme, Crit. Rev. Biochem. Mol. Biol. 43 (2008) 189–219.

[2] M. Kielian, Mechanisms of virus membrane fusion proteins, *Annual Rev.* Virol. 1 (2014) 171–189.

[3] S.C. Harrison, Viral membrane fusion, Virology 479 (2015) 498–507.

[4] S. Boonstra, J.S. Blijleven, W.H. Roos, P.R. Onck, E. van der Giessen, A.M. van Oijen, Hemagglutinin-mediated membrane fusion: A biophysical perspective, Ann. Revs. Biophys. 47 (2018) 153–173.

[5] T. Tang, M. Bidon, J.A. Jaimes, G.R. Whittaker, S. Daniel, Coronavirus membrane fusion mechanism offers a potential target for antiviral development, Antivir. Res. 178 (2020), 104792.

[6] I.A. Wilson, J.J. Skehel, D.C. Wiley, Structure of the haemagglutinin membrane glycoprotein of influenza virus at 3 A resolution, Nature 289 (1981) 366–373.

[7] M. Pancera, T.Q. Zhou, A. Druz, I.S. Georgiev, C. Soto, J. Gorman, J.H. Huang, P. Acharya, G.Y. Chuang, G. Ofek, G.B.E. Stewart-Jones, J. Stuckey, R.T. Bailer, M. G. Joyce, M.K. Louder, N. Tumba, Y.P. Yang, B.S. Zhang, M.S. Cohen, B.F. Haynes, J.R. Mascola, L. Morris, J.B. Munro, S.C. Blanchard, W. Mothes, M. Connors, P. D. Kwong, Structure and immune recognition of trimeric pre-fusion HIV-1 Env, Nature 514 (2014) 455–461.

[8] A.B. Ward, I.A. Wilson, The HIV-1 envelope glycoprotein structure: nailing down a moving target, Immunol. Rev. 275 (2017) 21–32.

[9] R.N. Kirchdoerfer, C.A. Cottrell, N.S. Wang, J. Pallesen, H.M. Yassine, H.L. Turner, K.S. Corbett, B.S. Graham, J.S. McLellan, A.B. Ward, Pre-fusion structure of a human coronavirus spike protein, Nature 531 (2016) 118–121.

[10] D. Wrapp, N. Wang, K.S. Corbett, J.A. Goldsmith, C.-L. Hsieh, O. Abiona, B. S. Graham, J.S. McLellan, Cryo-EM structure of the 2019-nCoV spike in the prefusion conformation, Science 367 (2020) 1260–1263.

[11] J. Chen, J.J. Skehel, D.C. Wiley, A polar octapeptide fused to the N-terminal fusion peptide solubilizes the influenza virus HA(2) subunit ectodomain, Biochemistry 37 (1998) 13643–13649.

[12] N. Lev, Y. Fridmann-Sirkis, L. Blank, A. Bitler, R.F. Epand, R.M. Epand, Y. Shai, Conformational stability and membrane interaction of the full-length ectodomain of HIV-1 gp41: implication for mode of action, Biochemistry 48 (2009) 3166–3175.

[13] K. Sackett, M.J. Nethercott, R.F. Epand, R.M. Epand, D.R. Kindra, Y. Shai, D. P. Weliky, Comparative analysis of membrane-associated fusion peptide secondary structure and lipid mixing function of HIV gp41 constructs that model the early pre-hairpin intermediate and final hairpin conformations, J. Mol. Biol. 397 (2010) 301–315.

[14] H. Aydin, D. Al-Khooly, J.E. Lee, Influence of hydrophobic and electrostatic residues on SARS-coronavirus S2 protein stability: insights into mechanisms of general viral fusion and inhibitor design, Protein Sci. 23 (2014) 603–617.

[15] R. Ranaweera, P.U. Ratnayake, D.P. Weliky, The stabilities of the soluble ectodomain and fusion peptide hairpins of the Influenza virus hemagglutinin subunit II protein are positively correlated with membrane fusion, Biochemistry 57 (2018) 5480–5493.

[16] M. Caffrey, M. Cai, J. Kaufman, S.J. Stahl, P.T. Wingfield, D.G. Covell, A. M. Gronenborn, G.M. Clore, Three-dimensional solution structure of the 44 kDa ectodomain of SIV gp41, EMBO J. 17 (1998) 4572–4584.

[17] Z.N. Yang, T.C. Mueser, J. Kaufman, S.J. Stahl, P.T. Wingfield, C.C. Hyde, The crystal structure of the SIV gp41 ectodomain at 1.47 A resolution, J. Struct. Biol. 126 (1999) 131–144.

[18] J. Chen, J.J. Skehel, D.C. Wiley, N- and C-terminal residues combine in the fusion-pH influenza hemagglutinin HA$_2$ subunit to form an N cap that terminates the triple-stranded coiled coil, Proc. Natl. Acad. Sci. U. S. A. 96 (1999) 8967–8972.

[19] S. Duquerroy, A.N. Vigouroux, P.J.M. Rottier, F.A. Rey, B.J. Bosch, Central ions and lateral asparagine/glutamine zippers stabilize the post-fusion hairpin conformation of the SARS coronavirus spike glycoprotein, Virology 335 (2005) 276–285.

[20] A.C. Walls, M.A. Tortorici, B. Snijder, X. Xiong, B.-J. Bosch, F.A. Rey, D. Veesler, Tectonic conformational changes of a coronavirus spike glycoprotein promote membrane fusion, Proc. Natl. Acad. Sci. U. S. A. 114 (2017) 11157–11162.

[21] L.V. Chernomordik, M.M. Kozlov, Mechanics of membrane fusion, Nat. Struct. Mol. Biol. 15 (2008) 675–683.

[22] R. Blumenthal, S. Durell, M. Viard, HIV entry and envelope glycoprotein-mediated fusion, J. Biol. Chem. 287 (2012) 40841–40849.

[23] P. Durrer, C. Galli, S. Hoenke, C. Corti, R. Gluck, T. Vorherr, J. Brunner, H+-induced membrane insertion of influenza virus hemagglutinin involves the HA2

amino-terminal fusion peptide but not the coiled coil region, J. Biol. Chem. 271 (1996) 13417–13421.

[24] S.R. Durell, I. Martin, J.M. Ruysschaert, Y. Shai, R. Blumenthal, What studies of fusion peptides tell us about viral envelope glycoprotein-mediated membrane fusion, Mol. Membr. Biol. 14 (1997) 97–112.

[25] X. Han, L.K. Tamm, A host-guest system to study structure-function relationships of membrane fusion peptides, Proc. Natl. Acad. Sci. U. S. A. 97 (2000) 13097–13102.

[26] L.H. Jia, S. Liang, K. Sackett, L. Xie, U. Ghosh, D.P. Weliky, REDOR solid-state NMR as a probe of the membrane locations of membrane-associated peptides and proteins, J. Magn. Reson. 253 (2015) 154–165.

[27] R.M. Epand, Fusion peptides and the mechanism of viral fusion, Biochim. Biophys. Acta 1614 (2003) 116–121.

[28] M. Ge, J.H. Freed, Fusion peptide from influenza hemagglutinin increases membrane surface order: An electron-spin resonance study, Biophys. J. 96 (2009) 4925–4934.

[29] C.M. Gabrys, R. Yang, C.M. Wasniewski, J. Yang, C.G. Canlas, W. Qiang, Y. Sun, D. P. Weliky, Nuclear magnetic resonance evidence for retention of a lamellar membrane phase with curvature in the presence of large quantities of the HIV fusion peptide, Biochim. Biophys. Acta 1798 (2010) 194–201.

[30] S. Tristram-Nagle, R. Chan, E. Kooijman, P. Uppamoochikkal, W. Qiang, D. P. Weliky, J.F. Nagle, HIV fusion peptide penetrates, disorders, and softens T-cell membrane mimics, J. Mol. Biol. 402 (2010) 139–153.

[31] H.W. Yao, M. Hong, Membrane-dependent conformation, dynamics, and lipid Interactions of the fusion peptide of the paramyxovirus PIV5 from solid-state NMR, J. Mol. Biol. 425 (2013) 563–576.

[32] S.T. Smrt, A.W. Draney, J.L. Lorieau, The influenza hemagglutinin fusion domain is an amphipathic helical hairpin that functions by inducing membrane curvature, J. Biol. Chem. 290 (2015) 228–238.

[33] H. Chakraborty, B.R. Lentz, M. Kombrabail, G. Krishnamoorthy, A. Chattopadhyay, Depth-dependent membrane ordering by Hemagglutinin fusion peptide promotes fusion, J. Phys. Chem. B 121 (2017) 1640–1648.

[34] A.L. Lai, J.H. Freed, HIV gp41 fusion peptide increases membrane ordering in a cholesterol-dependent fashion, Biophys. J. 106 (2014) 172–181.

[35] A.L. Lai, J.K. Millet, S. Daniel, J.H. Freed, G.R. Whittaker, The SARS-CoV fusion peptide forms an extended bipartite membrane platform that perturbs membrane order in a calcium-dependent manner, J. Mol. Biol. 429 (2017) 3875–3892.

[36] W.T. Heller, P.A. Zolnierczuk, The helix-to-sheet transition of an HIV-1 fusion peptide derivative changes the mechanical properties of lipid bilayer membranes, Biochim. Biophys. Acta 1861 (2019) 565–572.

[37] U. Ghosh, D.P. Weliky, ^{2}H nuclear magnetic resonance spectroscopy supports larger amplitude fast motion and interference with lipid chain ordering for membrane that contains beta sheet human immunodeficiency virus gp41 fusion peptide or helical hairpin influenza virus hemagglutinin fusion peptide at fusogenic pH, Biochim. Biophys. Acta 1862 (2020), 183404.

[38] U. Ghosh, D.P. Weliky, Rapid ^{2}H NMR transverse relaxation of perdeuterated lipid acyl chains of membrane with bound viral fusion peptide supports large-amplitude motions of these chains that can catalyze membrane fusion, Biochemistry 60 (2021) 2637–2651.

[39] E.O. Freed, E.L. Delwart, G.L. Buchschacher Jr., A.T. Panganiban, A mutation in the human immunodeficiency virus type 1 transmembrane glycoprotein gp41 dominantly interferes with fusion and infectivity, Proc. Natl. Acad. Sci. U. S. A. 89 (1992) 70–74.

[40] H. Qiao, R.T. Armstrong, G.B. Melikyan, F.S. Cohen, J.M. White, A specific point mutant at position 1 of the influenza hemagglutinin fusion peptide displays a hemifusion phenotype, Mol. Biol. Cell 10 (1999) 2759–2769.

[41] I.G. Madu, S.L. Roth, S. Belouzard, G.R. Whittaker, Characterization of a highly conserved domain within the Severe Acute Respiratory Syndrome coronavirus spike protein S2 domain with characteristics of a viral fusion peptide, J. Virol. 83 (2009) 7411–7421.

[42] I.G. Madu, S. Belouzard, G.R. Whittaker, SARS-coronavirus spike S2 domain flanked by cysteine residues C822 and C833 is important for activation of membrane fusion, Virology 393 (2009) 265–271.

[43] M. Rokonujjaman, A. Sahyouni, R. Wolfe, L. Jia, U. Ghosh, D.P. Weliky, A large HIV gp41 construct with trimer-of-hairpins structure exhibits V2E mutation-dominant attenuation of vesicle fusion and helicity very similar to V2E attenuation of HIV fusion and infection and supports: (1) hairpin stabilization of membrane apposition with larger distance for V2E; and (2) V2E dominance by an antiparallel β sheet with interleaved fusion peptide strands from two gp41 trimers, Biophys. Chem. 293 (2023), 106933.

[44] C.S. Kim, R.F. Epand, E. Leikina, R.M. Epand, L.V. Chernomordik, The final conformation of the complete ectodomain of the HA2 subunit of Influenza Hemagglutinin can by itself drive low pH-dependent fusion, J. Biol. Chem. 286 (2011) 13226–13234.

[45] W.R. Gallaher, Detection of a fusion peptide sequence in the transmembrane protein of human immunodeficiency virus, Cell 50 (1987) 327–328.

[46] E. Nobusawa, T. Aoyama, H. Kato, Y. Suzuki, Y. Tateno, K. Nakajima, Comparison of complete amino acid sequences and receptor binding properties among 13 serotypes of hemagglutinins of influenza A viruses, Virology 182 (1991) 475–485.

[47] J.L. Lorieau, J.M. Louis, A. Bax, The complete influenza hemagglutinin fusion domain adopts a tight helical hairpin arrangement at the lipid:water interface, Proc. Natl. Acad. Sci. U. S. A. 107 (2010) 11341–11346.

[48] U. Ghosh, L. Xie, L.H. Jia, S. Liang, D.P. Weliky, Closed and semiclosed interhelical structures in membrane vs closed and open structures in detergent for the Influenza Virus hemagglutinin fusion peptide and correlation of hydrophobic surface area with fusion catalysis, J. Am. Chem. Soc. 137 (2015) 7548–7551.

[49] P. Larsson, P.M. Kasson, Lipid tail protrusion in simulations predicts fusogenic activity of influenza fusion peptide mutants and conformational models, PLoS Comp. Biol. 9 (2013), e1002950.

[50] S. Legare, P. Lagueue, The influenza fusion peptide promotes lipid polar head intrusion through hydrogen bonding with phosphates and N-terminal membrane insertion depth, Proteins-Struc. Func. Bioinform. 82 (2014) 2118–2127.

[51] B.L. Victor, D. Lousa, J.M. Antunes, C.M. Soares, Self-assembly molecular dynamics simulations shed light into the interaction of the influenza fusion peptide with a membrane bilayer, J. Chem. Inf. Model. 55 (2015) 795–805.

[52] A. Pabis, R.J. Rawle, P.M. Kasson, Influenza hemagglutinin drives viral entry via two sequential intramembrane mechanisms, Proc. Natl. Acad. Sci. U. S. A. 117 (2020) 7200–7207.

[53] R. Worch, J. Krupa, A. Filipek, A. Szymaniec, P. Setny, Three conserved C-terminal residues of influenza fusion peptide alter its behavior at the membrane interface, Biochim. Biophys. Acta 1861 (2017) 97–105.

[54] C.P. Jaroniec, J.D. Kaufman, S.J. Stahl, M. Viard, R. Blumenthal, P.T. Wingfield, A. Bax, Structure and dynamics of micelle-associated human immunodeficiency virus gp41 fusion domain, Biochemistry 44 (2005) 16167–16180.

[55] C.M. Gabrys, D.P. Weliky, Chemical shift assignment and structural plasticity of a HIV fusion peptide derivative in dodecylphosphocholine micelles, Biochim. Biophys. Acta 1768 (2007) 3225–3234.

[56] W. Qiang, M.L. Bodner, D.P. Weliky, Solid-state NMR spectroscopy of human immunodeficiency virus fusion peptides associated with host-cell-like membranes: 2D correlation spectra and distance measurements support a fully extended conformation and models for specific antiparallel strand registries, J. Am. Chem. Soc. 130 (2008) 5459–5471.

[57] S.D. Schmick, D.P. Weliky, Major antiparallel and minor parallel beta sheet populations detected in the membrane-associated Human Immunodeficiency Virus fusion peptide, Biochemistry 49 (2010) 10623–10635.

[58] C.M. Gabrys, W. Qiang, Y. Sun, L. Xie, S.D. Schmick, D.P. Weliky, Solid-state nuclear magnetic resonance measurements of HIV fusion peptide ^{13}CO to lipid ^{31}p proximities support similar partially inserted membrane locations of the a Helical and b sheet peptide structures, J. Phys. Chem. A 117 (2013) 9848–9859.

[59] J.J. Buffy, T. Hong, S. Yamaguchi, A.J. Waring, R.I. Lehrer, M. Hong, Solid-state NMR investigation of the depth of insertion of protegrin-1 in lipid bilayers using paramagnetic Mn^{2+}, Biophys. J. 85 (2003) 2363–2373.

[60] Y. Su, R. Mani, M. Hong, Asymmetric insertion of membrane proteins in lipid bilayers by solid-state NMR paramagnetic relaxation enhancement: a cell-penetrating peptide example, J. Am. Chem. Soc. 130 (2008) 8856–8864.

[61] G.M. Clore, J. Iwahara, Theory, practice, and applications of paramagnetic relaxation enhancement for the characterization of transient low-population states of biological macromolecules and their complexes, Chem. Rev. 109 (2009) 4108–4139.

[62] T.M. Ferreira, F. Coreta-Gomes, O.H.S. Ollila, M.J. Moreno, W.L.C. Vaz, D. Topgaard, Cholesterol and POPC segmental order parameters in lipid membranes: solid state ^{1}H–^{13}C NMR and MD simulation studies, Phys. Chem. Chem. Phys. 15 (2013) 1976–1989.

[63] J. Schaefer, E.O. Stejskal, Carbon-13 nuclear magnetic resonance of polymers spinning at magic angle, J. Am. Chem. Soc. 98 (1976) 1031–1032.

[64] G. Metz, M. Ziliox, S.O. Smith, Towards quantitative CP-MAS NMR, Solid State Nucl. Magn. Reson. 7 (1996) 155–160.

[65] D. Huster, K. Arnold, K. Gawrisch, Investigation of lipid organization in biological membranes by two-dimensional nuclear Overhauser enhancement spectroscopy, J. Phys. Chem. B 103 (1999) 243–251.

[66] S.L. Veatch, O. Soubias, S.L. Keller, K. Gawrisch, Critical fluctuations in domain-forming lipid mixtures, Proc. Natl. Acad. Sci. U. S. A. 104 (2007) 17650–17655.

[67] W.L.C. Vaz, R.M. Clegg, D. Hallmann, Translational diffusion of lipids in liquid-crystalline phase phophatidylcholine bilayers. A comparison of experiment with theory, Biochemistry 24 (1985) 781–786.

[68] G. Oradd, G. Lindblom, NMR studies of lipid lateral diffusion in the DMPC/gramicidin D/water system: peptide aggregation and obstruction effects, Biophys. J. 87 (2004) 980–987.

[69] G. Lindblom, G. Oradd, Lipid lateral diffusion and membrane heterogeneity, Biochim. Biophys. Acta 1788 (2009) 234–244.

[70] J. Yang, P.D. Parkanzky, M.L. Bodner, C.G. Duskin, D.P. Weliky, Application of REDOR subtraction for filtered MAS observation of labeled backbone carbons of membrane-bound fusion peptides, J. Magn. Reson. 159 (2002) 101–110.

[71] C.M. Wasniewski, P.D. Parkanzky, M.L. Bodner, D.P. Weliky, Solid-state nuclear magnetic resonance studies of HIV and influenza fusion peptide orientations in membrane bilayers using stacked glass plate samples, Chem. Phys. Lipids 132 (2004) 89–100.

[72] Y. Sun, Secondary structure and membrane insertion of the membrane-associated Influenza fusion peptide probed by solid-state nuclear magnetic resonance, Ph. D. Thesis, Michigan State University, East Lansing, MI, USA, 2009.

[73] L. Janosi, A.A. Gorfe, Simulating POPC and POPC/POPG bilayers: conserved packing and altered surface reactivity, J. Chem. Theory Comput. 6 (2010) 3267–3273.

[74] E.A. Golovina, A.V. Golovin, F.A. Hoekstra, R. Faller, Water replacement hypothesis in atomic detail-Factors determining the structure of dehydrated bilayer stacks, Biophys. J. 97 (2009) 490–499.

[75] D.K. Chang, S.F. Cheng, C.H. Lin, E.A.B. Kantchev, C.W. Wu, Self-association of glutamic acid-rich fusion peptide analogs of influenza hemagglutinin in the membrane-mimic environments: Effects of positional difference of glutamic acids on side chain ionization constant and intra- and inter-peptide interactions deduced from NMR and gel electrophoresis measurements, Biochim. Biophys. Acta 1712 (2005) 37–51.

[76] P. Meier, E. Ohmes, G. Kothe, Multipulse dynamic nuclear magnetic resonance of phospholipid membranes, J. Chem. Phys. 85 (1986) 3598–3614.

[77] R.S. Prosser, J.H. Davis, C. Mayer, K. Weisz, G. Kothe, Deuterium NMR relaxation studies of peptide-lipid interactions, Biochemistry 31 (1992) 9355–9363.

[78] M.L. Bodner, C.M. Gabrys, P.D. Parkanzky, J. Yang, C.A. Duskin, D.P. Weliky, Temperature dependence and resonance assignment of ^{13}C NMR spectra of selectively and uniformly labeled fusion peptides associated with membranes, Magn. Reson. Chem. 42 (2004) 187–194.

[79] H.A. Scheidt, K. Kolocaj, J.V. Kristensen, D. Huster, D. Langosch, Transmembrane helix induces membrane fusion through lipid binding and splay, J. Phys. Chem. Lett. 9 (2018) 3181–3186.

Supplementary Material for "*Lipid acyl chain protrusion induced by the influenza virus hemagglutinin fusion peptide detected by NMR paramagnetic relaxation enhancement*"

Yijin Zhang, Ujjayini Ghosh, Li Xie, Daniel Holmes, Kathryn G. Severin, and David P. Weliky*
Department of Chemistry, Michigan State University, East Lansing, MI, 48824, USA

Figure S1. (**a**) Electrospray ionization mass spectrum of Fp and (**b**) expansion of z=+3 region. The calculated Fp mass is 2738 Da and peak regions in **a** are assigned to charge (z) states. Panel **b** shows clusters of isotopomer peaks with assignments of higher mass clusters to adducts with Na^+ and K^+ ions replacing H^+.
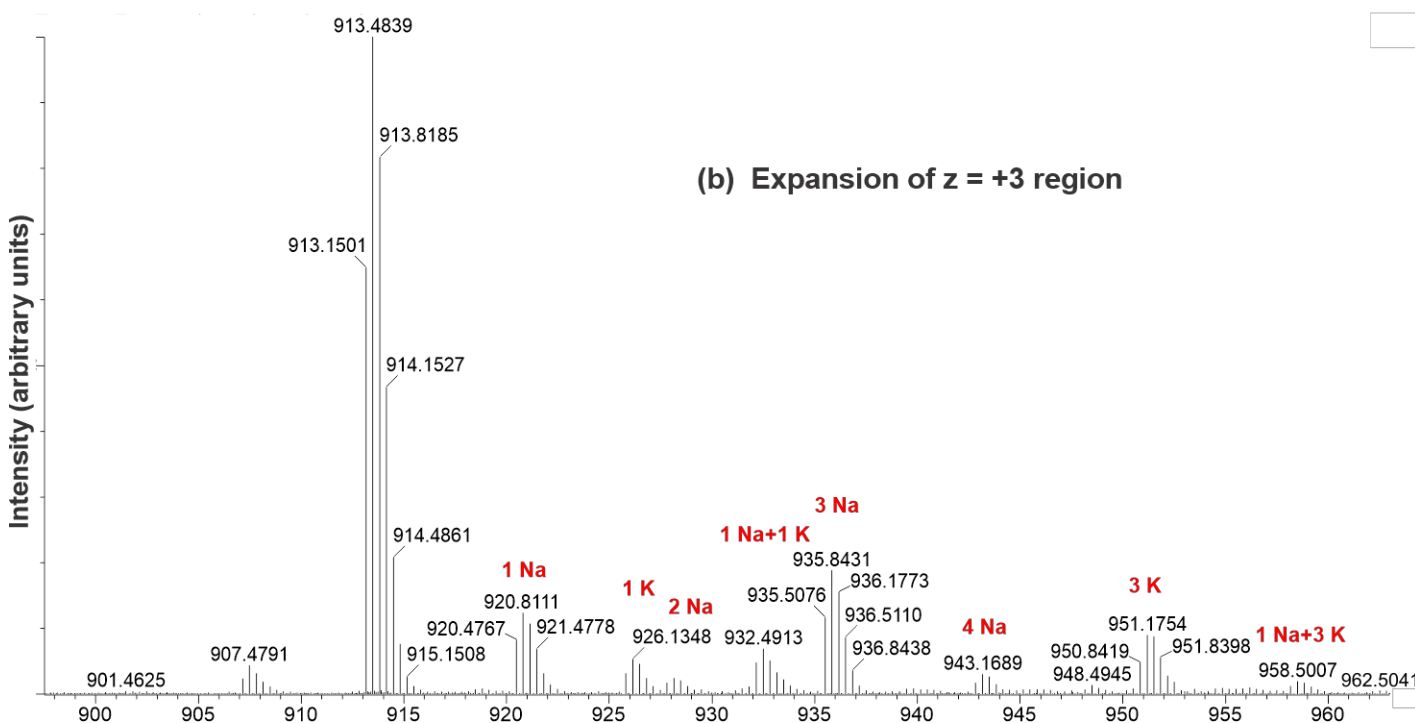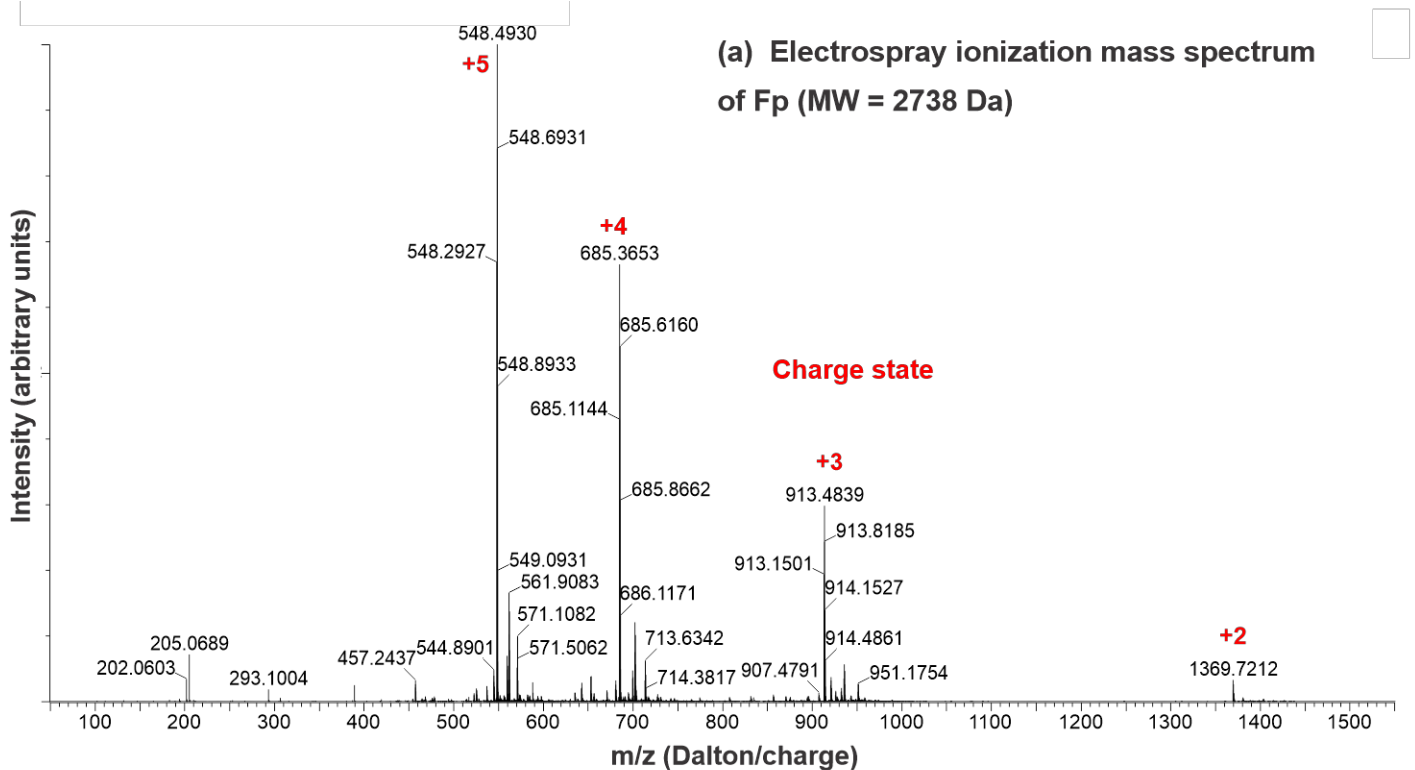
Figure S2. *1, *2, and *3 integration ranges
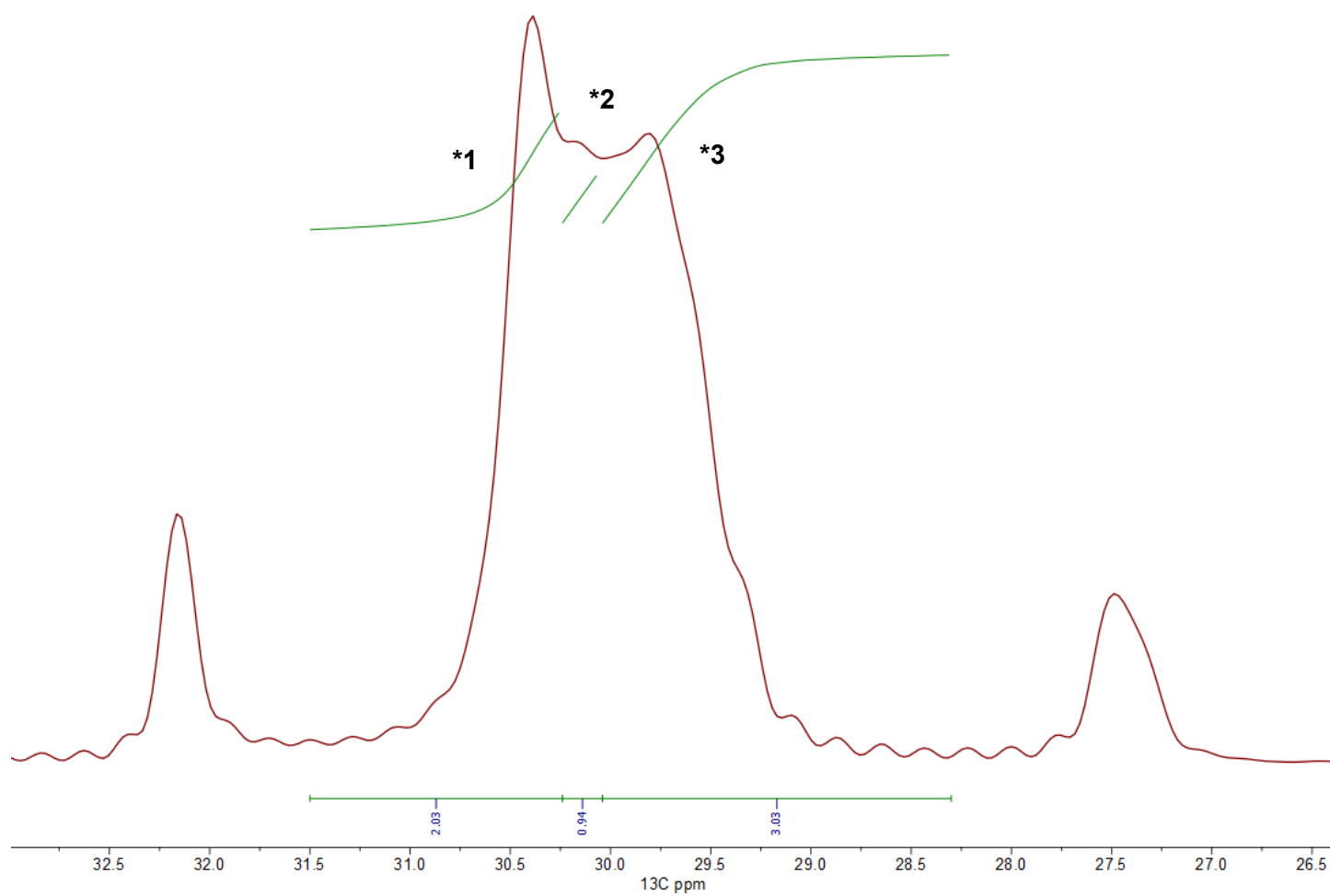
Figure S3. Plots of ln(Integrated peak intensity) vs. dephasing time (τ) and linear fitting for the Lipid, Lipid + Mn^{2+}, Lipid + Fp, and Lipid + Fp + Mn^{2+} samples. Data and fittings are displayed for the (a) 2,2′; (b) 3,3′; (c) 9,10; and (d) * peaks. The * peak is a superposition of signals from the 4-7, 12-15, and 4′-13′ sites. The plots of Integrated peak intensity vs. τ and exponential decay fitting are presented in Fig. 7 in the main manuscript.
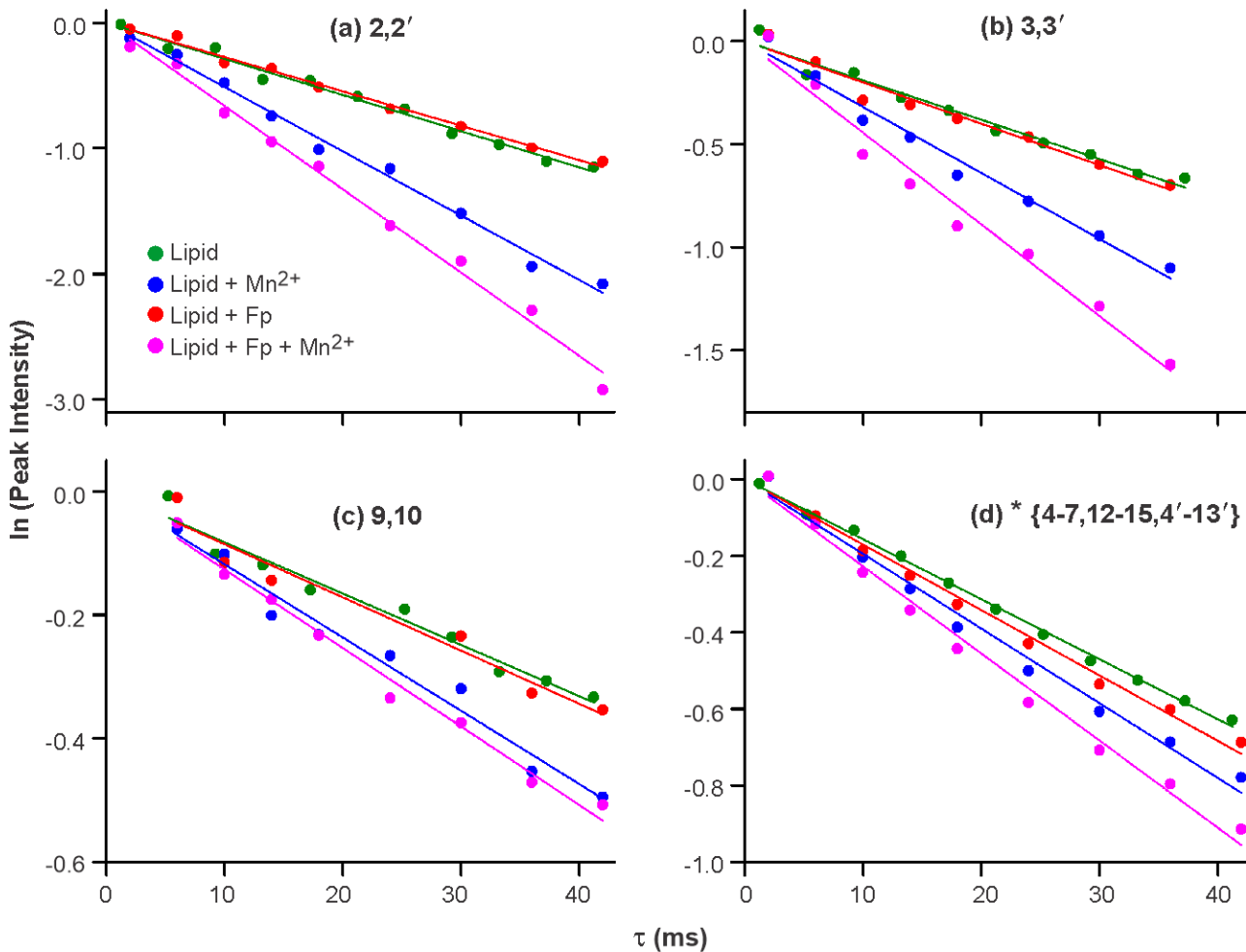
Table S1. Site-specific ^{13}C R_2's of acyl chains of POPC:POPG (4:1) membrane and Mn^{2+} dependence (fitting uncertainties in parentheses) [a]

| ^{13}C	%Mn^{2+}				
	0	0.5	0.75	1.00	1.25
2,2′	28.9(1.0)	50.4(1.8)	79.8(3.3)	91.9(3.6)	97.4(5.9)
3,3′	20.0(1.2)	35.6(2.4)	56.6(3.8)	63.0(4.1)	68.0(4.7)
8,11	9.2(0.7)	12.5(1.0)	18.2(1.1)	18.9(1.3)	21.5(1.5)
9,10	9.4(0.9)	12.5(0.8)	19.6(1.8)	21.8(2.1)	21.5(1.3)
16,14′	15.3(0.7)	15.1(0.6)	18.0(1.1)	21.8(1.3)	22.1(1.1)
17,15′	6.8(1.4)	6.6(0.9)	9.9(1.3)	10.9(1.9)	10.5(1.6)
* [4-7, 12-15, 4′-13′]	15.8(0.3)	20.6(0.9)	26.1(1.0)	28.5(1.4)	29.3(1.3)
*1 [6′-9′]	23.7(0.2)	30.5(0.4)	34.4(0.4)	36.2(1.1)	36.1(0.7)
*2 [7,10′,11′]	15.1(0.2)	16.4(0.8)	23.3(1.0)	25.2(1.4)	25.8(1.3)
*3 [4-6,12-15, 4′,5′,12′,13′]	11.0(0.3)	15.4(1.0)	20.4(1.4)	22.6(1.6)	24.4(1.7)

[a] Each ^{13}C transverse relaxation rate (R_2) was determined from best-fitting the integrated NMR peak intensity S vs. delay time τ using S = A $\times$ exp(-$R_2 \times \tau$) where A and R_2 are fitting parameters. The fitting uncertainty of R_2 is given in parentheses. The * peak is the superposition of the 4-7, 12-15, and 4′-13′ signals. Typical ppm integration ranges for peaks are: 2,2′, 33.00-37.00; 3,3′, 24.00-26.30; 8,11, 26.50-28.20; 9,10, 128.00-131.00; 16,14′, 31.50-33.00; 17,15′, 21.50-23.60; *, 28.30-31.50; *1, 30.24-31.50; *2, 30.04-30.24; *3, 28.30-30.04 (Fig. S2). The ^{13}C sites that make the largest contributions to the *1, *2, and *3 integration ranges are listed between the brackets. The % Mn^{2+} = (mole bound Mn^{2+})/(mole lipid) $\times$ 100.

Table S2. Site-specific ^{13}C Γ_2's of acyl chains of POPC:POPG (4:1) and Mn^{2+} dependence (uncertainties in parentheses) [a]

^{13}C	%Mn^{2+}			
	0.5	0.75	1.00	1.25
2,2′	21.5(2.1)	51.0(3.5)	63.0(3.8)	68.6(6.0)
3,3′	15.6(2.7)	36.5(4.0)	42.9(4.3)	47.9(5.0)
8,11	3.2(1.2)	8.9(1.3)	9.7(1.4)	12.3(1.6)
9,10	3.1(1.2)	10.2(2.0)	12.4(2.3)	12.1(1.5)
16,14′	-0.2(0.9)	2.7(1.3)	6.5(1.5)	6.8(1.3)
17,15′	-0.2(1.6)	3.1(1.9)	4.1(2.4)	3.7(2.1)
* [4-7, 12-15, 4′-13′]	4.7(0.9)	10.3(1.1)	12.7(1.5)	13.5(1.4)
*1 [6′-9′]	6.8(0.5)	10.6(0.5)	12.5(1.1)	12.4(0.7)
*2 [7,10′,11′]	1.3(0.9)	8.2(1.0)	10.1(1.5)	10.7(1.4)
*3 [4-6,12-15, 4′,5′,12′,13′]	4.4(1.1)	9.3(1.4)	11.5(1.6)	13.4(1.8)

[a] The Γ_2 values are the differences between the best-fit R_2 values of samples with vs. without Mn^{2+} (Table S1) and the fitting uncertainty of Γ_2 is given in parentheses. The % Mn^{2+} = (mole bound Mn^{2+})/(mole lipid) $\times$ 100.

Table S3. Site-specific ^{13}C transverse relaxation rates of acyl chains of POPC:POPG (4:1) membrane and Mn^{2+} and Fp dependences, with fitted values for replicate datasets (fitting uncertainties in parentheses) [a]

^{13}C	R_2 (s^{-1})							
	w/o Fp, w/o Mn^{2+}		w/o Fp, 0.5% Mn^{2+}		3% Fp, w/o Mn^{2+}		3% Fp, 0.5% Mn^{2+}	
	Rep. 1	Rep. 2	Rep. 1	Rep. 2	Rep. 1	Rep. 2	Rep. 1	Rep. 2
2,2′	28.8(1.4)	30.9(1.2)	51.5(2.1)	50.4(1.8)	28.1(1.2)	31.2(1.2)	63.5(3.2)	64.0(6.0)
3,3′	20.0(1.5)	15.8(1.4)	35.2(2.4)	35.6(2.4)	21.3(2.0)	20.1(1.6)	51.1(4.0)	53.8(2.2)
8,11	9.1(0.7)	8.0(0.9)	12.6(0.9)	12.5(0.8)	13.6(1.6)	11.8(1.5)	19.8(1.7)	22.8(1.0)
9,10	8.4(0.6)	9.0(1.0)	11.9(0.8)	12.5(1.0)	8.7(1.0)	13.9(1.2)	13.0(1.2)	18.5(1.9)
16,14′	15.5(0.7)	13.5(0.8)	15.0(0.6)	15.1(0.6)	13.8(0.8)	16.7(0.8)	15.4(0.7)	18.9(1.0)
17,15′	5.9(0.7)	5.8(0.9)	7.3(0.4)	6.6(0.9)	8.6(0.8)	8.6(1.1)	9.7(1.0)	11.8(1.3)
* [4-7, 12-15, 4′-13′]	15.8(0.3)	15.1(0.7)	20.5(0.9)	20.6(0.9)	17.8(0.7)	19.0(0.8)	24.1(1.1)	27.9(0.4)
*1 [6′-9′]	24.8(0.2)	24.4(0.3)	27.2(1.5)	30.9(0.4)	25.4(0.5)	30.2(0.3)	30.3(0.3)	34.7(1.6)
*2 [7,10′,11′]	15.1(0.2)	13.6(0.7)	16.4(0.9)	16.4(0.8)	16.0(0.7)	17.3(0.6)	23.2(1.0)	26.7(0.4)
*3 [4-6,12-15, 4′,5′,12′,13′]	11.7(0.3)	10.9(0.9)	18.8(0.9)	15.4(1.0)	15.8(1.2)	14.4(1.0)	23.1(1.8)	24.3(0.8)

[a] Each ^{13}C transverse relaxation rate (R_2) was determined from best-fitting the integrated NMR peak intensity S vs. delay time τ using $S(\tau) = A \times \exp(-R_2 \times \tau)$ where A and R_2 are fitting parameters. The fitting uncertainty of R_2 is given in parentheses. The R_2's are given for fitting of replicate datasets, Rep. 1 and Rep. 2, with Rep. 1 values reported in Table 2 in the main manuscript. Typical ppm integration ranges for peaks are: 2,2′, 33.00-37.00; 3,3′, 24.00-26.30; 8,11, 26.50-28.20; 9,10, 128.00-131.00; 16,14′, 31.50-33.00; 17,15′, 21.50-23.60; *, 28.30-31.50; *1, 30.24-31.50; *2, 30.04-30.24; *3, 28.30-30.04 (Fig. S2). The ^{13}C sites that make the largest contributions to the *1, *2, and *3 integration ranges are listed between the brackets. The % Mn^{2+} = (mole bound Mn^{2+})/(mole lipid) $\times$ 100. The % Fp is calculated using the same type of expression. The replicate datasets for w/o Fp, 0.5% Mn^{2+} are different processings of the same datasets, i.e. different phasings and baseline corrections. The other replicate datasets are for different acquired spectra.

Table S4. Site-specific ^{13}C transverse relaxation rates of acyl chains of POPC:POPG (4:1) membrane with 3% Fp and without Mn^{2+}, with fitted values for replicate samples (fitting uncertainties in parentheses) [a]

^{13}C	R$_2$ (s^{-1})	
	Samp. 1	Samp. 2
2,2′	28.1(1.2)	37.3(1.5)
3,3′	21.3(2.0)	20.3(1.2)
8,11	13.6(1.6)	10.7(1.0)
9,10	8.7(1.0)	11.6(1.4)
16,14′	13.8(0.8)	19.9(1.0)
17,15′	8.6(0.8)	9.3(1.4)
* [4-7, 12-15, 4′-13′]	17.8(0.7)	18.4(0.5)
*1 [6′-9′]	25.4(0.5)	32.5(0.6)
*2 [7,10′,11′]	16.0(0.7)	16.4(0.4)
*3 [4-6,12-15, 4′,5′,12′,13′]	15.8(1.2)	13.9(0.5)

[a] Each ^{13}C transverse relaxation rate (R$_2$) was determined from best-fitting the integrated NMR peak intensity S vs. delay time τ using $S(\tau) = A \times exp(-R_2 \times \tau)$ where A and R$_2$ are fitting parameters. The fitting uncertainty of R$_2$ is given in parentheses. The R$_2$'s are given for fitting of data from replicate samples, Samp. 1 and Samp. 2, with Samp. 1 values reported in Table 2 in the main manuscript. Typical ppm integration ranges for peaks are: 2,2′, 33.00-37.00; 3,3′, 24.00-26.30; 8,11, 26.50-28.20; 9,10, 128.00-131.00; 16,14′, 31.50-33.00; 17,15′, 21.50-23.60; *, 28.30-31.50; *1, 30.24-31.50; *2, 30.04-30.24; *3, 28.30-30.04 (Fig. S2). The ^{13}C sites that make the largest contributions to the *1, *2, and *3 integration ranges are listed between the brackets.